

1-1-2016

A One-Hole Cu₄S Cluster with N₂O Reductase Activity: A Structural and Functional Model for Cu_Z

Brittany J. Johnson
University of Illinois at Chicago

William E. Antholine
Medical College of Wisconsin

Sergey Lindeman
Marquette University, sergey.lindeman@marquette.edu

Michael J. Graham
Northwestern University

Neal P. Mankad
University of Illinois at Chicago

A One-Hole Cu_4S Cluster with N_2O Reductase Activity: A Structural and Functional Model for Cu_Z^*

Brittany J. Johnson

*Department of Chemistry, University of Illinois at Chicago,
Chicago, IL*

William E. Antholine

*Department of Biophysics, Medical College of Wisconsin,
Milwaukee, WI*

Sergey V. Lindeman

*Department of Chemistry, Marquette University,
Milwaukee, WI*

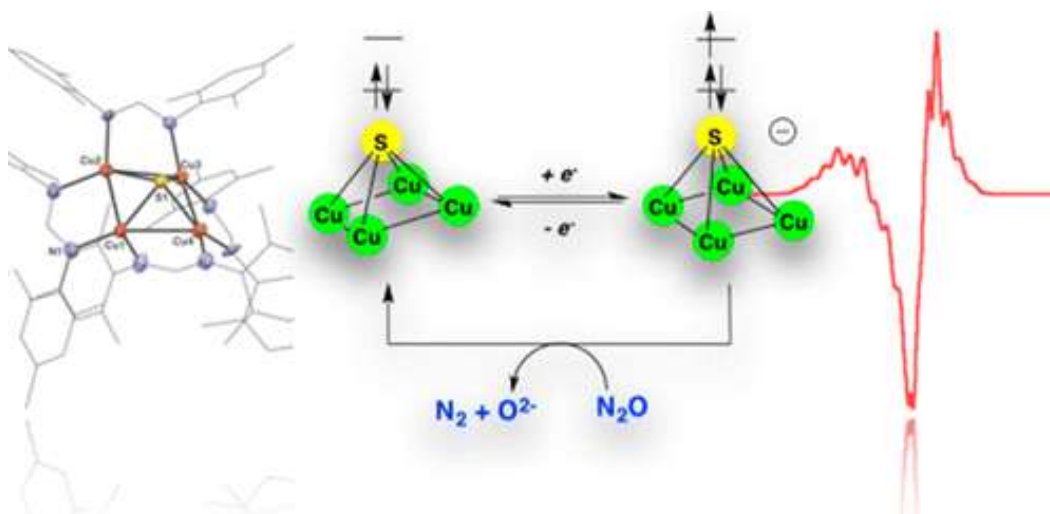
Michael J. Graham

*Department of Chemistry, Northwestern University,
Evanston, IL*

Neal P. Mankad

*Department of Chemistry, University of Illinois at Chicago,
Chicago, IL*

Abstract



During bacterial denitrification, two-electron reduction of N₂O occurs at a [Cu₄(μ₄-S)] catalytic site (Cu₂^{*}) embedded within the nitrous oxide reductase (N₂OR) enzyme. In this Communication, an amidinate-supported [Cu₄(μ₄-S)] model cluster in its one-hole (S = 1/2) redox state is thoroughly characterized. Along with its two-hole redox partner and fully reduced clusters reported previously, the new species completes the two-electron redox series of [Cu₄(μ₄-S)] model complexes with catalytically relevant oxidation states for the first time. More importantly, N₂O is reduced by the one-hole cluster to produce N₂ and the two-hole cluster, thereby completing a closed cycle for N₂O reduction. Not only is the title complex thus the best structural model for Cu₂^{*} to date, but it also serves as a functional Cu₂^{*} mimic.

Regulation of nitrous oxide (N₂O) concentration in the atmosphere is crucial due to N₂O's key roles both as an anthropogenic greenhouse gas and as an ozone layer depletion agent.^{1,2} Lessons can be taken from nature, where atmospheric N₂O concentrations are regulated by the bacterial denitrification metalloenzyme, nitrous oxide reductase (N₂OR).³ The catalytic site in N₂OR that is reactive under biological conditions is Cu₂^{*},⁴ a [Cu₄(μ₄-S)] cluster characterized in the resting "one-hole" (3Cu^I:1Cu^{II}, S = 1/2) state^{5,6} and active in the "fully reduced" (4Cu^I, S = 0) state (Figure 1a).⁷ Under certain conditions, the Cu₂^{*} site in N₂OR is replaced by Cu_Z,⁸ a [Cu₄(μ₄-S)(μ₂-S)] cluster with a "two-hole" (2Cu^I:2Cu^{II}, S = 0) resting state that converts to a [Cu₄(μ₄-S)(μ₂-SH)] cluster upon reduction to the one-hole state, which shows relevant though limited N₂O reductase activity (Figure 1b).⁹ Because N₂OR catalyzes the two-electron reduction of N₂O, three Cu₂^{*}

redox states (4Cu^{I} , $3\text{Cu}^{\text{I}}:1\text{Cu}^{\text{II}}$, and $2\text{Cu}^{\text{I}}:2\text{Cu}^{\text{II}}$) spanning a two-electron range are plausibly relevant to catalysis.^{10,11}

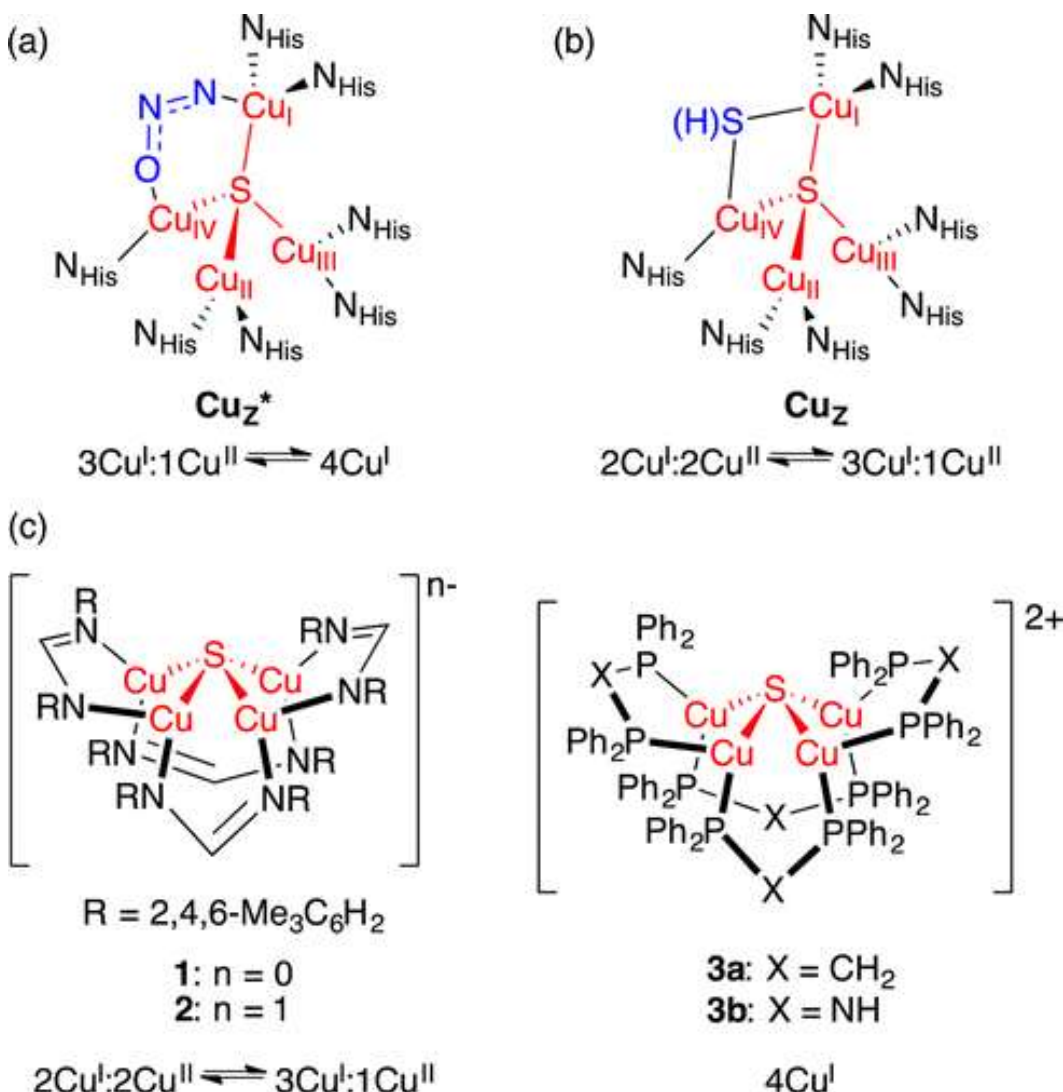
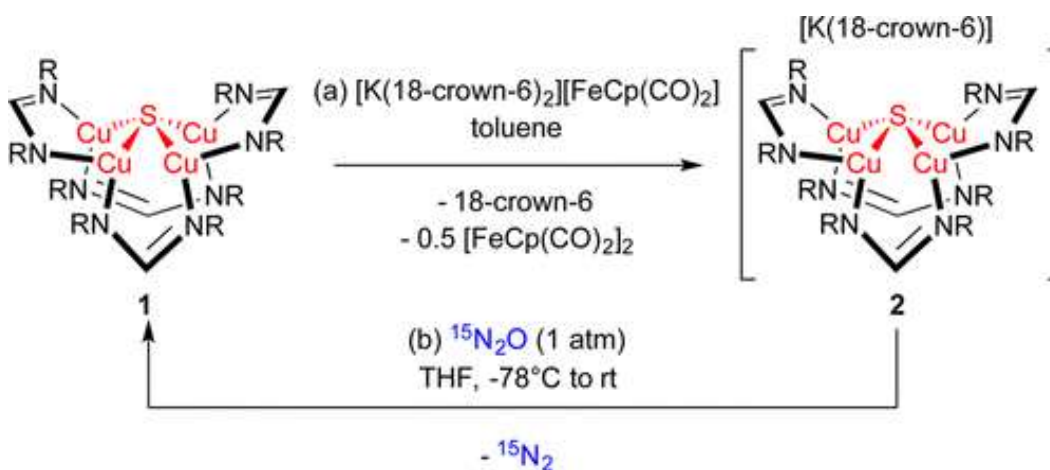


Figure 1. Structures of (a) Cu_2^* (with N_2O bound) and (b) Cu_2 sites of N_2OR . (c) $[\text{Cu}_4(\mu_4\text{-S})]$ model complexes.

The unique $[\text{Cu}_4(\mu_4\text{-S})]$ structural motif and the rich redox chemistry of this catalytic site have presented challenges to synthetic modeling chemistry. Synthetic examples of $[\text{Cu}_4(\mu_4\text{-S})]$ clusters supported by phosphorus ligands have only been isolated in the 4Cu^{I} state and do not react with N_2O .^{12,13} Other relevant models that do access open-shell oxidation states feature $[\text{Cu}_3(\mu_3\text{-S}_2)]$ or $[\text{Cu}_3(\mu_3\text{-S})]$ cores that do not structurally model Cu_2^* .^{14,15} Similarly, functional models capable of N_2O reduction feature $[\text{Cu}_3(\mu_2\text{-S}_2)]$ or $[\text{Cu}_2(\mu_2\text{-SR})]$

cores,^{16,17} limiting mechanistic insight to be gained for comparison to the tetracopper core of Cu_z^* .

We recently reported a $[\text{Cu}_4(\mu_4\text{-S})]$ cluster (**1**), supported by nitrogenous amidinate ligands,¹⁸ that was characterized in its two-hole state. Here, we report the synthesis and characterization of its one-electron reduction product, the one-hole derivative (**2**). Along with the fully reduced clusters supported by diphosphine¹² (**3a**) and diphosphinous amide¹³ (**3b**) ligands, this completes the catalytically relevant two-electron redox series of $[\text{Cu}_4(\mu_4\text{-S})]$ model complexes for the first time (Figure 1c). Species **2** reduces N_2O stoichiometrically, producing **1** + N_2 and completing a synthetic cycle for N_2O reduction (Scheme 1). The **1/2** redox pair thus represents both a structural and functional Cu_z^* model system.



Scheme 1. Synthetic Cycle for N_2O Reduction

We previously showed that cluster **1** assembles upon addition of S-atom donors to a dicopper(I) bis(amidinate) precursor.¹⁸ The two-hole, formally $2\text{Cu}^{\text{I}}:2\text{Cu}^{\text{II}}$ complex **1** was originally assigned as having a $S = 0$ ground state and a low-lying $S = 1$ excited state, the latter based on detection of a temperature-dependent solution magnetic moment and an EPR signal with non-Curie behavior. However, analysis of rigorously purified samples of **1** by SQUID magnetometry reveal near-zero χ_T values up to 400 K (Figures S1), consistent with a diamagnetic species. Furthermore, one of the side products formed during assembly of **1** was characterized by X-ray crystallography. This monocopper(II) species resulting from S-atom insertion into two Cu–N bonds (Figure S2) gives an EPR signal matching that previously

reported for **1** (Figure S3). Rigorously purified samples of **1**, on the other hand, are EPR-silent. Considering these new data, we now assign **1** as being diamagnetic, while data consistent with paramagnetism in previous samples are now assigned to trace impurities.

Complex **1** possesses a reversible one-electron redox event at $E^{\circ'} = -1.28$ V vs Fc^+/Fc ($\text{Fc} = \text{ferrocene}$).¹⁸ Chemical reduction of **1** with $[\text{K}(18\text{-crown-6})_2][\text{Fp}]$ ($\text{Fp} = \text{FeCp}(\text{CO})_2$, $E^{\circ'} = -1.8$ V vs Fc^+/Fc)¹⁹ produced **2** as its $[\text{K}(18\text{-crown-6})]^+$ salt, along with 1 equiv of free 18-crown-6 and 0.5 equiv of Fp_2 (Scheme 1a). X-ray crystallographic analysis of **2** revealed two symmetrically independent tetracopper anions, one of which is shown in Figure 2. Both anions feature close contacts between an amidinate mesityl ring and the nearby $[\text{K}(18\text{-crown-6})]^+$ unit. Anionic **2** is isostructural to **1** and to dicationic **3a** and **3b**, with local C_{2v} symmetry and an alternating up-down-up-down pattern for the bridging amidinates.

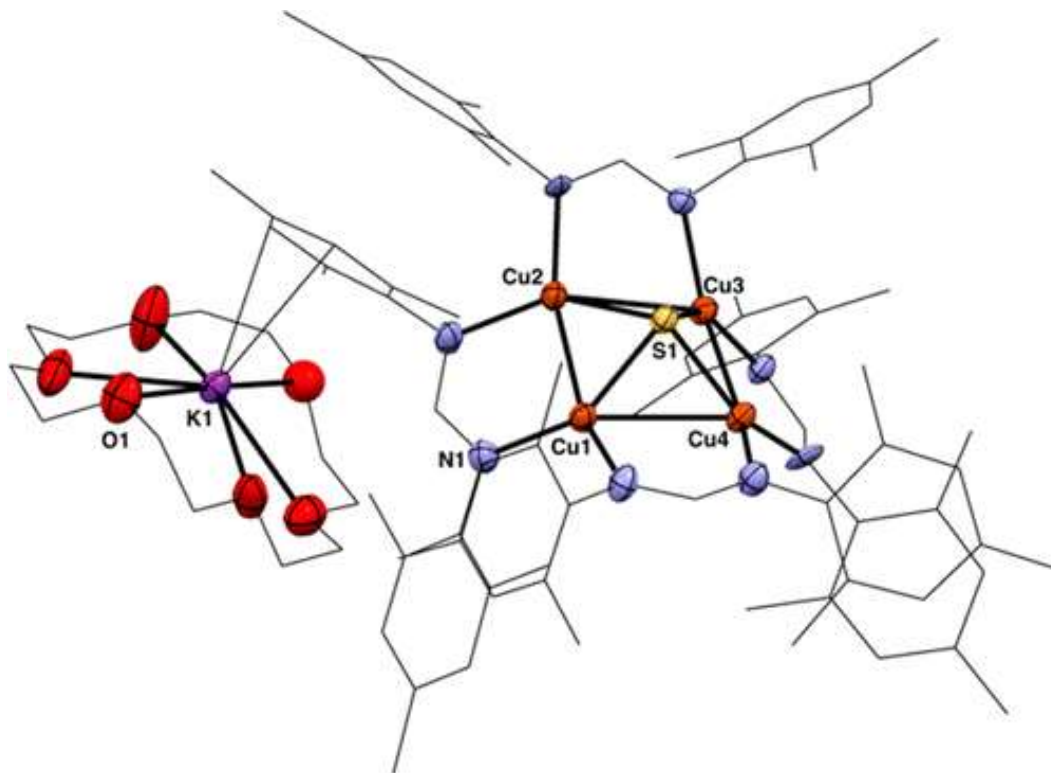
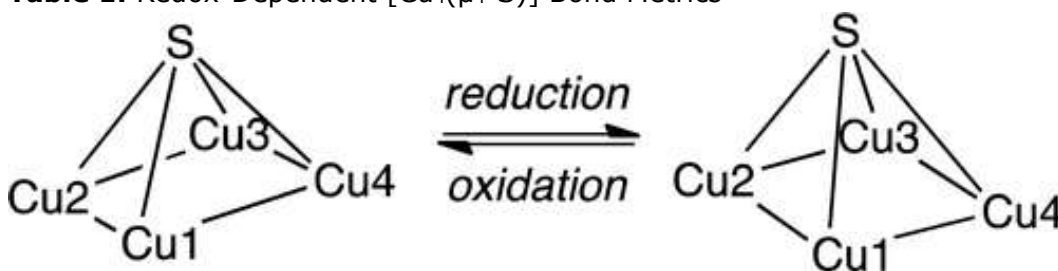


Figure 2. Solid-state structure of anionic **2** as a $[\text{K}(18\text{-crown-6})]^+$ salt. Hydrogen atoms, co-crystallized solvent, and a symmetrically independent second molecule have been omitted for clarity.

Key structural parameters for the pyramidal $[\text{Cu}_4(\mu_4\text{-S})]$ pentahedra within **1**, **2**, and **3a** are compared in [Table 1](#). The two-hole species **1** features a rectangular Cu_4 base, with alternating short and long Cu–Cu distances. Upon reduction to one-hole **2**, the Cu_4 base is less unsymmetric and approaches a square shape, with a smaller difference between short and long Cu–Cu distances. The core of fully reduced **3a** is even closer to a square-based pyramid shape. Evidently, there is a well-behaved pattern across the redox series: the Cu_4 base gets more rectangular with increasing oxidation level, and gets more square with decreasing oxidation level. The geometry of the four-coordinate S center is less well behaved as a function of redox state, as measured by the τ_4 parameter²⁰ that does not follow a clear pattern across the series. The $[\text{Cu}_4(\mu_4\text{-S})]$ core of one-hole Cu_z^* has a seesaw shape rather than a pyramidal shape, with nearest-neighbor Cu–Cu distances spanning 2.56–3.36 Å.²¹

Table 1. Redox-Dependent $[\text{Cu}_4(\mu_4\text{-S})]$ Bond Metrics^a



	1 (two-hole)^b	2 (one-hole)^c	3a (0-hole)^d
Cu1–Cu2	2.4226(6)	2.502(1)	2.869(1)
Cu2–Cu3	3.0353(6)	2.809(1)	3.128(1)
Cu3–Cu4	2.4226(6)	2.532(1)	2.869(1)
Cu1–Cu4	3.0353(6)	2.831(1)	3.128(1)
$\tau_4(\text{S})^e$	0.76	0.90	0.59

^aBond distances in Å.

^bFrom ref [18](#).

^cFor one of two molecules in the asymmetric unit.

^dFrom ref [12](#).

^eFor $\mu_4\text{-S}$ ligand: τ_4 is 1.00 for T_d and 0.00 for D_{4h} , see ref [20](#).

The $S = 1/2$ species **2** was characterized by X-band and Q-band EPR spectroscopy. The g -values for the axial signal were not readily obtained from the X-band spectrum ([Figure 3a](#)) but were well resolved in the Q-band spectrum ([Figure S4](#)): $g_{\perp} = 2.090$ and $g_{\parallel} = 2.043$. Resolved lines on the high- and low-field sides of the X-band spectrum ([Figure S5](#)) were attributed to Cu hyperfine splitting, and values of A_{\perp}

= 100 MHz and $A_{\parallel} = 15$ MHz were obtained by fitting the X-band and Q-band spectra. The second-derivative X-band spectrum emphasizes fine structure for the 13-line pattern resulting from four equivalent Cu centers, and the simulated spectrum fits the experimental data well (Figure 3b). The Cu hyperfine coupling in **2** is small in magnitude relative to that of typical cupric species. A previous one-hole $[\text{Cu}_3(\mu_3\text{-S})]$ model exhibited an isotropic signal ($g = 2.095$) with a similarly small Cu hyperfine constant (97 MHz).¹⁵ The EPR signatures for one-hole Cu_z^* and Cu_z are distinct from that of **2** in that they have $g_{\parallel} > g_{\perp}$ and larger hyperfine constants (Table 2).⁹

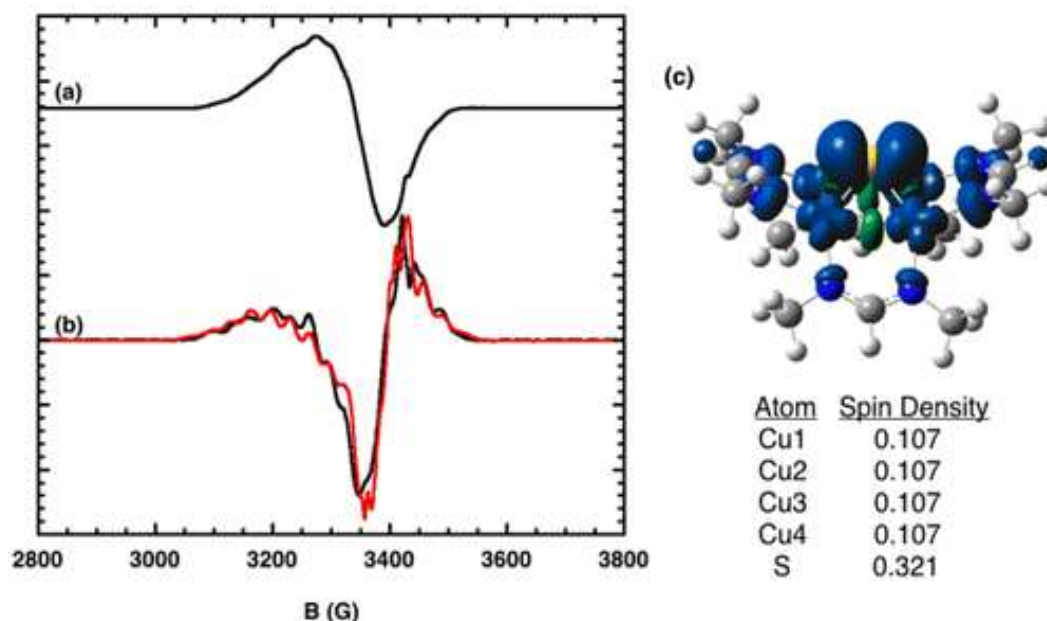


Figure 3. X-band EPR data (9.632 GHz, 9.9 K, 2-MeTHF) for **2** shown as (a) first derivative and (b) second-derivative overlay of simulation (red) and experiment (black). (c) Mulliken spin density plot (0.001 isovalue) for **2'** calculated by DFT.

Table 2. Redox-Dependent Spectroscopic Properties

	1 ^a	2	Cu_z ^{b,c}	Cu_z ^{b,d}	Cu_z* ^{b,d}
g_{\parallel}		2.043		2.152	2.160
g_{\perp}		2.090		2.042	2.043
A_{\parallel} ^e		15		168	182, 69
A_{\perp} ^e		100		60	75, 60
λ_{max} ^f	561 (470) ^h	566	546 (670) ^h	694	680
ϵ^g	14 000 ⁱ	8600	10 000 ⁱ	3000	4500

^aFrom ref 18.

^bFrom ref 9.

^cTwo-hole.

^dOne-hole.

^eIn MHz.

^fIn nm.

^gIn M⁻¹ cm⁻¹.

^hShoulder.

ⁱFor main peak.

Based on the EPR data for **2**, the formally 3Cu^I:1Cu^{II}:S²⁻ complex can be viewed as an admixture of two limiting resonance contributors: a delocalized 4Cu^{1.25}:S²⁻ mixed-valent species, and a 4Cu^I:S⁻ sulfur-radical species. To our knowledge, the literature of sulfur EPR spectroscopy does not include any four-coordinate examples for comparison to the S center in **2**.²²⁻²⁴ To probe the electronic structure further, we analyzed a model complex **2'**, in which the mesityl groups had been replaced with methyl groups, using DFT computations. The computed bond distances within the [Cu₄(μ₄-S)] core for **2'** matched experimental values well ([Table S1](#)). The Mulliken spin density for **2'** was found to be delocalized, with equal populations on each of the four Cu centers and with the S center having the most spin density (32%) of any single atom ([Figure 3c](#)). This computational observation indicates a high degree of covalency in the [Cu₄(μ₄-S)] core.

Complexes **1** and **2** are purple. Complex **1** features a strong absorbance at 561 nm ($\epsilon = 14\,000\text{ M}^{-1}\text{ cm}^{-1}$) with a shoulder at 470 nm.¹⁸ Upon reduction ([Figure 4a](#)), this feature shifted slightly in **2** to 566 nm and got measurably less intense ($\epsilon = 8600\text{ M}^{-1}\text{ cm}^{-1}$). Absorption data for Cu_z* are available only for the one-hole state. Cu_z has been characterized in both its two-hole and one-hole states ([Table 2](#)): a large red-shift and a decrease in intensity are observed upon reduction,⁹ and these transitions previously have been attributed to S²⁻-to-Cu charge transfer.

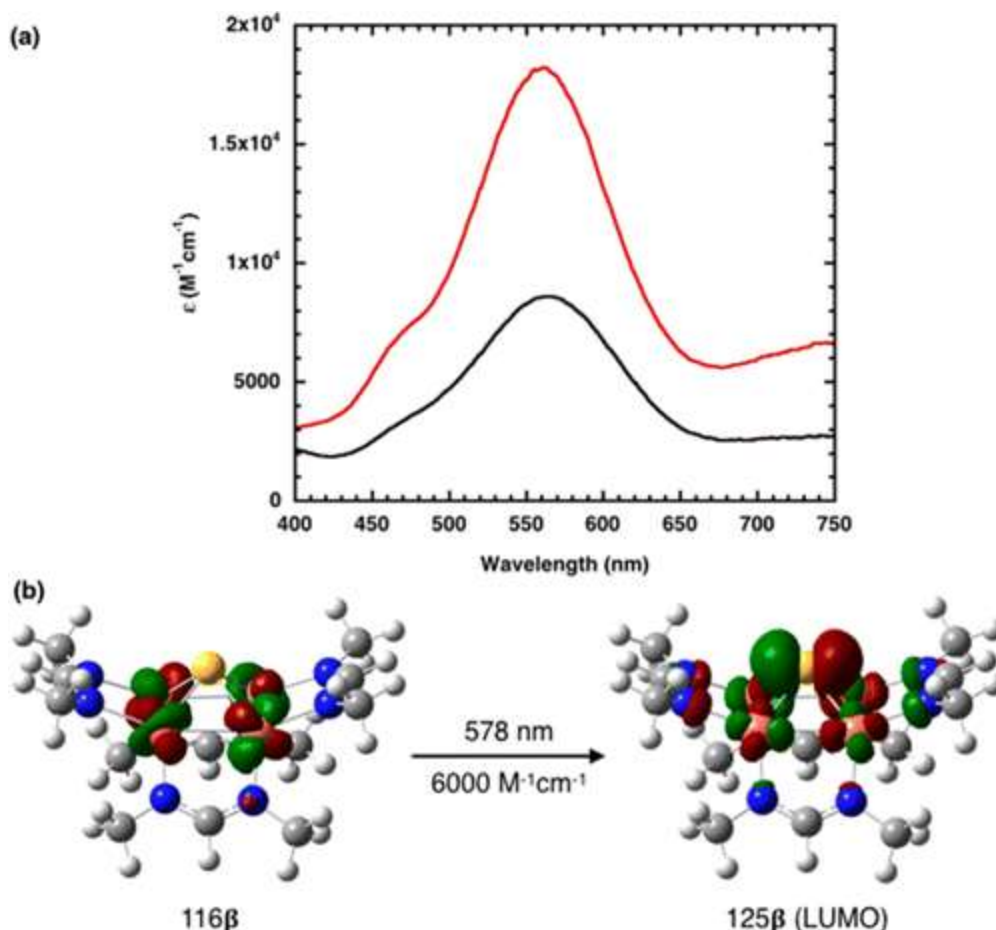
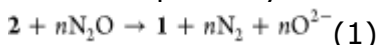


Figure 4. (a) UV-vis data for **1** (red) and **2** (black). (b) Natural transition orbitals (0.04 isovalues) for 578 nm excitation of **2'** calculated by TD-DFT. Relative contributions to NTO 125β : S, 23%; Cu, 14% each.

TD-DFT calculations for **2'** predicted a characteristic feature at 578 nm ($\epsilon = 6000 \text{ M}^{-1} \text{ cm}^{-1}$), and natural transition orbital (NTO) analysis²⁵ indicated that this transition involves excitation of a β -electron from NTO 116β to NTO 125β (Figure 4b). NTO 116β is predominantly a linear combination of four Cu $3d_{xz}$ orbitals, while NTO 125β (the LUMO) has significant S $3p_x$ character. The dominant electronic transition thus clearly involves charge transfer from the four Cu centers to the S center and resembles a delocalized Cu $3d$ -to-Cu-S σ^* transition. TD-DFT calculations for **1'** correctly predicted an increase in intensity (to $\epsilon = 16000 \text{ M}^{-1} \text{ cm}^{-1}$) and the presence of a shoulder, though not the lack of energy shift.

A reaction was observed when solutions of **2** were exposed to N_2O (1 atm) at $-78 \text{ }^\circ\text{C}$. ^1H NMR analysis indicated that **2** had been

oxidized to **1** in up to 89% yield (Scheme 1b). Under certain conditions, evolution of N₂ was detected by headspace GC-MS analysis and comparison to control reactions in the absence of **2** under identical experimental conditions. Evolution of ¹⁵N₂ was detected when ¹⁵N₂O was used, verifying that the liberated nitrogen derived from nitrous oxide. Addition of electrophiles Me₃SiCl or PhC(O)Cl to the final product mixtures produced (Me₃Si)₂O or PhC(O)OC(O)Ph, consistent with the presence of nucleophilic O²⁻. Collectively, these observations establish that the reaction shown in eq 1 was taking place. Due to difficulties in accurately quantifying the N₂ and O²⁻ produced, the value of *n* in eq 1 is ambiguous at this time. Our working hypothesis is that two molecules of **2** cooperate to reduce N₂O by two electrons, with one cluster activating the N₂O substrate and the other acting as a sacrificial reductant. Regardless, complex **2** is the first synthetic [Cu₄S] complex to exhibit N₂O reactivity, and thus it opens a new avenue of investigation in N₂O reductase research. Ongoing studies in our laboratory are aimed at detecting intermediates along the N₂O reduction pathway and elucidating the reduction mechanism.



In conclusion, the first one-hole [Cu₄(μ₄-S)] complex has been synthesized and thoroughly characterized, completing the two-electron redox series of [Cu₄(μ₄-S)] model complexes. Structural, spectroscopic, and computational evidence is consistent with highly covalent bonding within the [Cu₄(μ₄-S)] core. This redox-active [Cu₄(μ₄-S)] system is also a functional mimic for Cu_z*, participating in a synthetic cycle for N₂O reduction. The title compound thus can be viewed as both a structural and functional model for Cu_z*.

The authors declare no competing financial interest.

Acknowledgment

Funds to N.P.M. were provided by NIH/NIGMS (R01 GM116820), the UIC Department of Chemistry, and a Sloan Research Fellowship. EPR facilities are supported by NIH (National Biomedical EPR Center Grant EB001980). SQUID measurements were funded by the International Institute for Nanotechnology (State of Illinois DCEO Award 10-203031) and Northwestern University. Prof. Yoshitaka Ishii (UIC) provided access to a UV-vis spectrometer, and Prof. Danna Freedman (Northwestern) to a SQUID magnetometer. Yeni Yung

assisted with headspace GC-MS analysis. Prof. Justin Walensky (Missouri) generously shared unpublished data relevant to [Figure S2](#).

References

- ¹Thomson, A. J.; Giannopoulos, G.; Pretty, J.; Baggs, E. M.; Richardson, D. J. *Philos. Trans. R. Soc., B* 2012, 367, 1157, DOI: 10.1098/rstb.2011.0415
- ²Ravishankara, A. R.; Daniel, J. S.; Portmann, R. W. *Science* 2009, 326, 123, DOI: 10.1126/science.1176985
- ³Pauleta, S. R.; Dell'Acqua, S.; Moura, I. *Coord. Chem. Rev.* 2013, 257, 332, DOI: 10.1016/j.ccr.2012.05.026
- ⁴Johnston, E. M.; Dell'Acqua, S.; Ramos, S.; Pauleta, S. R.; Moura, I.; Solomon, E. I. *J. Am. Chem. Soc.* 2014, 136, 614, DOI: 10.1021/ja411500p
- ⁵Chen, P.; Cabrito, I.; Moura, J. J. G.; Moura, I.; Solomon, E. I. *J. Am. Chem. Soc.* 2002, 124, 10497, DOI: 10.1021/ja0205028
- ⁶Ghosh, S.; Gorelsky, S. I.; DeBeer George, S.; Chan, J. M.; Cabrito, I.; Dooley, D. M.; Moura, J. J. G.; Moura, I.; Solomon, E. I. *J. Am. Chem. Soc.* 2007, 129, 3955, DOI: 10.1021/ja068059e
- ⁷Ghosh, S.; Gorelsky, S. I.; Chen, P.; Cabrito, I.; Moura; Moura, I.; Solomon, E. I. *J. Am. Chem. Soc.* 2003, 125, 15708, DOI: 10.1021/ja038344n
- ⁸Pomowski, A.; Zumft, W. G.; Kroneck, P. M. H.; Einsle, O. *Nature* 2011, 477, 234, DOI: 10.1038/nature10332
- ⁹Johnston, E. M.; Dell'Acqua, S.; Pauleta, S. R.; Moura, I.; Solomon, E. I. *Chem. Sci.* 2015, 6, 5670, DOI: 10.1039/C5SC02102B
- ¹⁰Gorelsky, S. I.; Ghosh, S.; Solomon, E. I. *J. Am. Chem. Soc.* 2006, 128, 278, DOI: 10.1021/ja055856o
- ¹¹Solomon, E. I.; Heppner, D. E.; Johnston, E. M.; Ginsbach, J. W.; Cirera, J.; Qayyum, M.; Kieber-Emmons, M. T.; Kjaergaard, C. H.; Hadt, R. G.; Tian, L. *Chem. Rev.* 2014, 114, 3659, DOI: 10.1021/cr400327t
- ¹²Yam, V. W.-W.; Lee, W.-K.; Lai, T.-F. *J. Chem. Soc., Chem. Commun.* 1993, 1571, DOI: 10.1039/C39930001571
- ¹³Johnson, B. J.; Lindeman, S. V.; Mankad, N. P. *Inorg. Chem.* 2014, 53, 10611, DOI: 10.1021/ic501720h
- ¹⁴Brown, E. C.; York, J. T.; Antholine, W. E.; Ruiz, E.; Alvarez, S.; Tolman, W. B. *J. Am. Chem. Soc.* 2005, 127, 13752, DOI: 10.1021/ja053971t
- ¹⁵Di Francesco, G. N.; Gaillard, A.; Ghiviriga, I.; Abboud, K. A.; Murray, L. J. *Inorg. Chem.* 2014, 53, 4647, DOI: 10.1021/ic500333p
- ¹⁶Bar-Nahum, I.; Gupta, A. K.; Huber, S. M.; Ertem, M. Z.; Cramer, C. J.; Tolman, W. B. *J. Am. Chem. Soc.* 2009, 131, 2812, DOI: 10.1021/ja808917k

- ¹⁷Esmieu, C.; Orio, M.; Torelli, S.; Le Pape, L.; Pécaut, J.; Lebrun, C.; Ménage, S. *Chem. Sci.* 2014, 5, 4774, DOI: 10.1039/C4SC01487A
- ¹⁸Johnson, B. J.; Antholine, W. E.; Lindeman, S. V.; Mankad, N. P. *Chem. Commun.* 2015, 51, 11860, DOI: 10.1039/C5CC04675K
- ¹⁹Connelly, N. G.; Geiger, W. E. *Chem. Rev.* 1996, 96, 877, DOI: 10.1021/cr940053x
- ²⁰Yang, L.; Powell, D. R.; Houser, R. P. *Dalton Trans.* 2007, 955, DOI: 10.1039/B617136B
- ²¹Brown, K.; Tegoni, M.; Prudêncio, M.; Pereira, A. S.; Besson, S.; Moura, J. J.; Moura, I.; Cambillau, C. *Nat. Struct. Biol.* 2000, 7, 191, DOI: 10.1038/73288
- ²²Imada, Y.; Nakano, H.; Furukawa, K.; Kishi, R.; Nakano, M.; Maruyama, H.; Nakamoto, M.; Sekiguchi, A.; Ogawa, M.; Ohta, T.; Yamamoto, Y. *J. Am. Chem. Soc.* 2016, 138, 479, DOI: 10.1021/jacs.5b10774
- ²³van Gastel, M.; Lubitz, W.; Lassmann, G.; Neese, F. *J. Am. Chem. Soc.* 2004, 126, 2237, DOI: 10.1021/ja038813l
- ²⁴Hasegawa, A.; Williams, F. *Chem. Phys. Lett.* 1977, 45, 275, DOI: 10.1016/0009-2614(77)80268-6
- ²⁵Martin, R. L. *J. Chem. Phys.* 2003, 118, 4775, DOI: 10.1063/1.1558471

Supporting Information

The Supporting Information is available free of charge on the [ACS Publications website](https://pubs.acs.org) at DOI: [10.1021/jacs.6b05480](https://doi.org/10.1021/jacs.6b05480).

- Procedures and supporting data ([PDF](#))
- Crystallographic data ([CIF](#))

A 1-hole Cu₄S cluster with N₂O reductase activity: a structural and functional model for Cu_Z*

Brittany J. Johnson, William E. Antholine, Sergey V. Lindeman, Michael J. Graham,
Neal P. Mankad*

* npm@uic.edu

Supporting Information

Contents:

Experimental and preparation of compounds	S3
Reaction between 2 and N ₂ O	S7
Oxygen trapping experiments from reaction between 2 and N ₂ O	S8
Headspace Analysis by GC-MS of ¹⁵ N ₂ O and 2	S9
Computational methods	S10
Figure S1. χT vs. temperature plots of 1 ⁴	S12
Figure S2. X-ray crystal structure of Cu(II)S ₂ NCN ₂ paramagnetic impurity	S13
Figure S3. X-band EPR spectrum of Cu(II)S ₂ NCN ₂ impurity	S14
Figure S4. Q-band EPR spectrum of 2	S15
Figure S5. X-band EPR spectrum of 2	S16
Figure S6. ¹ H NMR of 2	S16
Figure S7. Absorption spectra for 0.082 mM 2 and 0.085 mM 1 ⁴ in THF	S17
Figure S8. Infrared spectrum of 2	S18
Figure S9. ¹ H NMR of 1 formed after exposure of N ₂ O to 2	S19
Figure S10. ¹ H NMR of control experiment between N ₂ and 2	S20
Figure S11. ¹ H NMR of recovered 1 after reaction with N ₂ O and 2	S21
Figure S12. ¹ H NMR of recovered 1 after control between N ₂ and 2	S22
Figure S13. ¹ H NMR of oxygen trapping using Me ₃ SiCl after N ₂ O and 2	S23
Figure S14. ¹ H NMR of oxygen trapping using Me ₃ SiCl after N ₂ and 2	S24

Figure S15. ^1H NMR of oxygen trapping using benzoyl chloride after N_2O and 2	S25
Figure S16. Comparison of ^1H NMR of oxygen trapping using benzoyl chloride to confirm formation of benzoic anhydride	S26
Figure S17. Reaction headspace chromatogram from $^{15}\text{N}_2\text{O}$ and 2	S27
Figure S18. $^{15}\text{N}_2\text{O}$ blank flask chromatogram	S28
Figure S19. Mass spectrum of $^{15}\text{N}_2\text{O}$ and 2 after 48 hours	S29
Table S1. Percent composition of species in Figure S19	S29
Figure S20. Mass spectrum of $^{15}\text{N}_2\text{O}$ blank after 48 hours	S30
Table S2. Percent composition of species in Figure S20	S30
Figure 21. Mass spectrum of $^{15}\text{N}_2\text{O}$ and 2 after 6 hours	S31
Table S3. Percent composition of species in Figure S21	S31
Figure S22. Mass spectrum of $^{15}\text{N}_2\text{O}$ blank	S32
Table S4. Percent composition of species in Figure S22	S32
Figure S23. Mass spectrum of elude at 5.48 minutes in Figure S17	S33
Table S5. Integration values of $^{15}\text{N}_2$ from reaction vs. blank headspace	S33
Table S6: Comparison of calculated and experimental bond distances	S34
Figure S24. Optimized structure of 2'	S35
Figure S25. Calculated UV-Vis spectrum of 2'	S35
Figure S26. Optimized structure of 1'	S36
Figure S27. Calculated UV-Vis spectrum of 1'	S36
Table S7. Optimized coordinates of 2'	S37
Table S8. Optimized coordinates of 1'	S39
Table S9. Excitation energies and oscillator strengths of 2'	S41
Table S10. Excitation energies and oscillator strengths of 1'	S45
Figures S28-29. Selected MO surfaces for 1'	S52
Figures S30-31. Selected MO surfaces for 2'	S53
References cited	S54

EXPERIMENTAL

General Considerations. Unless otherwise specified, all reactions and manipulations were performed under purified N₂ in a glovebox or using standard Schlenk line techniques. Glassware was oven-dried prior to use. Reaction solvents (diethyl ether, toluene, tetrahydrofuran, dichloromethane, acetonitrile, pentane) were sparged with argon and dried using a Glass Contour Solvent System built by Pure Process Technology, LLC. Deuterated solvents were degassed by repeated freeze-pump-thaw cycles and then stored over 3-Å molecular sieves. Unless otherwise specified, all other chemicals were purchased from commercial sources and used without further purification. 1 L of Nitrous Oxide (¹⁵N₂, 98%+) was purchased from Cambridge Isotope Laboratories, Inc. A 460 mL Stainless Steel 1/4" NPT Stainless Steel Whitey Straight/Male adaptor was also purchased and assembled from Cambridge Isotope Laboratories packaging prior to shipment.

Spectroscopic Measurements. NMR spectra for compound characterization were recorded at ambient temperature using Bruker Avance DPX-400 or Bruker Avance DRX-500 MHz spectrometers. ¹H NMR chemical shifts were referenced to residual solvent peaks. FT-IR spectra were recorded on solid samples in a glovebox using a Bruker ALPHA spectrometer fitted with a diamond-ATR detection unit. Elemental analyses were performed by the Midwest Microlab, LLC in Indianapolis, IN. UV-Vis absorbance spectra were taken at room temperature using a JASCO V-660 Spectrophotometer. Absorbance was measured at 0.5 nm intervals and with a continuous scan speed of 1000 nm/min. X-band spectra were obtained at 10 K with an Elexsys E500 spectrometer, Bruker, Billerica, MA located at the National Biomedical EPR Center at the Medical College of Wisconsin. Q-band spectra were obtained on a Varian E109 spectrometer at -150°C located at the National Biomedical EPR Center at the Medical College of Wisconsin. Spectra were

simulated with EasySpin.¹ The 1st harmonic spectra were obtained using SumSpec (a program available from the National Biomedical EPR Center) using pseudomodulation with a 1% or 3% Bessel function. Samples of 5 mM **1**⁴ (not shown), **2** and Cu(II)S₂NCN₂-containing impurity were glassed in 2-methyltetrahydrofuran.

Magnetic Measurements. Magnetic measurements were performed on polycrystalline samples in a sealed polyethylene bag or in a sealed quartz tube restrained with eicosane. All data were collected using a Quantum Design MPMS-XL SQUID magnetometer in a temperature range of 1.8 to 400 K at applied dc fields of 0.1 T and 7 T. A quartz tube was employed for high temperature measurements to avoid melting the polyethylene bag, and a high-field was employed with the quartz-tube sample to ensure sufficient signal-to-noise at high temperatures.

X-ray crystallography. X-ray crystallography data on dark violet tablets of **2** was collected at the X-ray Structural Laboratory at Marquette University (Milwaukee, WI). The X-ray single-crystal diffraction data were collected with an Oxford Diffraction SuperNova diffractometer equipped with dual microfocus Cu/Mo X-ray sources, X-ray mirror optics, Atlas CCD detector and low-temperature Cryojet device. Data was collected using Cu(K α) radiation at 100 K. The data was processed with CrysAlisPro program package (Oxford Diffraction Ltd., 2010) typically using a numerical Gaussian absorption correction (based on the real shape of the crystal) followed by an empirical multi-scan correction using SCALE3 ABSPACK routine. The structures were solved using SHELXS program and refined with SHELXL program² within Olex2 crystallographic package.³ All computations were performed on an Intel PC computer under Windows 7 OS. Hydrogen atoms were localized in difference syntheses of electron density but were refined using appropriate geometric restrictions on the corresponding bond lengths and bond angles within a riding/rotating model (torsion angles of Me hydrogens were optimized to better fit

the residual electron density). The crystal was twinned: regular twins with 180° rotation around direct -101 vector. Because of quasi-rational cell dimensions, all reflections with $h+l=2n$ overlap exactly (but not with identical indexes - HKL transformation matrix $\begin{pmatrix} -.5 & 0 & -.5 & 0 & -1 & 0 & -1.5 & 0 & .5 \end{pmatrix}$). Reflections with $h+l=2n+1$ are separate. The structure contains two symmetrically independent tetranuclear units having a similar geometry. Two K^+ /18-crown-6 counter ions are disordered to a different degree. The disorder affects as the position of K atom (swinging alternatively in axial direction to make $K^+ \dots Ar$ contacts with neighboring anions) as well as the crown-ether itself. The structure contains well-ordered 1 eq of solvate DCM solvent. It also contains large areas of highly-disordered solvent only partially localized/identified as diethyl ether. Because of the twinning, an application of a solvent mask procedure was prohibited.

Headspace Analysis by GC-MS. Headspace gas was analyzed by a JEOL GCMate II (JEOL USA, Peabody MA) gas chromatograph/mass spectrometer, the gas chromatograph was an Agilent 6890Plus (Wilmington DE) equipped with a G1513A autoinjector with 100 vial sample tray connected to a G1512A controller. The gas chromatography column was a J&W GS-CarbonPLOT (Agilent Tech), 60 m long, 0.320 mm diameter, 1.50 μm film thickness. The carrier gas was helium (99.999% Ultra High Purity) run through a STG triple filter (Restek Corp.) at a constant flow rate of 2.5 mL/min. The inlet temperature was 250°C and was fitted with an Agilent 4 mm ID single taper split liner containing deactivated glass wool. The static headspace analysis was performed using 5 μL of the experimental gas mixture manually injected via syringe. The GC inlet split ratio was 20:1. The GC oven was run in isothermal mode at a temperature of 30°C for 5 minutes then ramped $10^\circ\text{C}/\text{min}$ to 80°C . Total run time was approximately 10 min. The mass spectrometer was a benchtop magnetic sector operating at a nominal resolving power of 500 using an accelerating voltage of 2500 V. The spectrometer was operated in full scan EI mode (+Ve) with

the filament operating at 70 eV scanning from m/z 10 to m/z 850 using a linear magnet scan. The scan speed was 0.2 s/scan. Data analysis was performed using the TSSPro software (Shrader Analytical & Consulting Laboratories, Inc., Detroit MI) provided with the spectrometer. Mass calibration was performed using perfluorokerosene (PFK).

Preparation of $[\text{Cu}_4(\mu_4\text{-S})(\mu_2\text{-NCN})_4][\text{K}(18\text{-crown-6})]$ (2**).** **1**⁴ (0.10 g, 0.079 mmol) was dissolved in approximately 60 mL of toluene using a magnetic stir bar. Solid $[\text{K}(18\text{-crown-6})_2][\text{Fp}]^5$ (0.057 g, 0.076 mmol) was added slowly to stirring solution at room temperature. The solution was stirred vigorously overnight. The next day the solution was filtered. The collected dark solid was washed with pentane to remove any Fp_2 (cyclopentadienyliron dicarbonyl dimer) until filtrate was clear, and then washed with toluene to remove any unreacted **1** until filtrate was clear. The solid was collected and dried under vacuum. Yield of **2**: 0.091 g, 75%. Compound **2** was stored in a freezer (-36°C) and is not stable in solution at room temperature for more than an hour. Note: Trace amounts (2-5%) of $\text{Cu}_2[(2,4,6\text{-Me}_3\text{C}_6\text{H}_2\text{N})_2\text{C}(\text{H})]_2^4$ were often detected by ¹H NMR regardless of multiple purification attempts. The best method for removing $\text{Cu}_2[(2,4,6\text{-Me}_3\text{C}_6\text{H}_2\text{N})_2\text{C}(\text{H})]_2$ is by adding a small amount of tetrahydrofuran (2 mL) to solid **2** (0.091 g) so that $\text{Cu}_2[(2,4,6\text{-Me}_3\text{C}_6\text{H}_2\text{N})_2\text{C}(\text{H})]_2$ dissolves but **2** is super-saturated and doesn't dissolve entirely. This solution is filtered, and the resulting purple solid is washed with a small amount of tetrahydrofuran (2 mL) and then pentane (2 mL) to remove any remaining tetrahydrofuran solvent. The purple solid can then be collected and dried under vacuum. Usually this purification method is done once to achieve experimental purity. Dark black crystals may be obtained by dissolving **2** in a minimum amount of dimethoxyethane, pipette-filtering through Celite, and leaving solution at -36°C for four days. NMR samples were dissolved in acetone-*d*₆ and pipette-filtered through Celite into NMR tube. ¹H NMR (500 MHz, acetone-*d*₆): δ 3.66 (s, 24 H, 18-crown-6). FT-IR (cm⁻¹

¹): 2992, 2903, 2854, 2724, 1717, 1652, 1609, 1556, 1538, 1469, 1330, 1209, 1104, 959, 847, 738, 586, 504, 422. Anal. calcd. for C₈₈H₁₁₆Cu₄N₈O₆SK: C, 61.90; H, 6.85; N, 6.56. Found: C, 60.37; H, 6.50; N, 6.57. Repeated attempts at obtaining satisfactory combustion analysis results (with %C within ±0.4% of the calculated value) gave results with a large degree of variance, indicating either that the spectroscopically pure samples were compromised during shipping/handling or that the compound does not combust cleanly.

Detection of 1 after reaction between N₂O and 2. Inside a N₂ filled glovebox, to a Schlenk tube equipped with a Teflon screw cap and magnetic stir bar, **2** (0.006 g, 0.0035 mmol) was added and dissolved in approximately 2.5 mL dichloromethane. The tube was sealed with the Teflon screw cap and taken out of the glovebox and connected to a Schlenk line streaming N₂O. The solution was cooled to -78° C (dry ice and acetone bath) with stirring. The solution was then exposed to N₂O for 6.5 hours while maintaining the cooling bath at -78° C. Once cooling bath was removed, solvent was removed by vacuum evaporation and Schlenk tube was closed and pumped back into the glovebox. Evaporated residue was dissolved in CD₂Cl₂ and pipette-filtered through Celite into an NMR tube for analysis. A control experiment was conducted by same procedure using 0.005 g (0.0029 mmol) of **2** in approximately 2 mL of dichloromethane while under N₂. Using integration of 18-crown-6 as an internal standard (24 H) in ¹H NMR reveals 45% NMR yield of **1**⁴ in the reaction with N₂O (Figure S9) with respect to any Ar-CH₃ peak of **1** (12 H) and 0% yield in N₂ control experiment (Figure S10).

Recovery of 1 after reaction between N₂O and 2. Inside a N₂ filled glovebox, to a Schlenk tube equipped with a Teflon screw cap and magnet stir bar, **2** (0.021 g, 0.012 mmol) was added and dissolved in dichloromethane (10 mL). The tube was sealed with the Teflon cap and taken out of the glovebox and connected to Schlenk line streaming with N₂O. The solution in the

flask was cooled to -78°C (dry ice and acetone bath) with stirring, and then opened to N_2O for 6 hours while maintaining the cooling bath at -78°C . Solvent was removed by vacuum evaporation and Schlenk tube was closed and pumped back into the glovebox. Purple evaporated residue inside Schlenk tube was washed with acetonitrile (approximately 20 mL), in which **1** is insoluble, and then pipette-filtering through Celite until filtrate became clear. Dark purple solid remaining was collected using dichloromethane and the solution was completely evaporated by vacuum. The same procedure was followed in a control experiment using 0.021 g (0.012 mmol) of **2** in 10 mL of dichloromethane under N_2 . Amount of **1** isolated from N_2O reaction residue: 0.015 g (0.010 mmol, 88% yield, Figure S11); amount of **1** isolated from N_2 control reaction residue: 0.0052 g (0.0035 mmol, 30% decomposition, Figure S12).

Oxygen Trapping Experiment with Me_3SiCl . Inside a N_2 filled glovebox, to a Schlenk tube equipped with a Teflon screw cap and magnet stir bar, **2** (0.003 g, 0.0017 mmol) was added and dissolved in dichloromethane (3 mL). The tube was sealed with the Teflon cap and taken out of the glovebox and connected to Schlenk line streaming with N_2O . The solution in the flask was cooled to -78°C (dry ice and acetone bath) with stirring, and then opened to N_2O for 3.5 hours while maintaining the temperature at -78°C . Solvent was removed by vacuum evaporation and Schlenk tube was closed and pumped back into the glovebox. Purple evaporated residue inside Schlenk tube was dissolved in approximately 1 mL of CD_2Cl_2 , and 95 μL of a 0.092 M solution of TMS-Cl (0.0087 mmol) in CD_2Cl_2 was added. Contents were stirred for 1 hour at room temperature and were then pipette-filtered through Celite into an NMR tube for analysis (Figure S13). The same procedure was followed in a control experiment using 0.006 g (0.0035 mmol) of **2** in 3 mL of dichloromethane, under N_2 , followed by addition of 190 μL of 0.092 M TMS-Cl in CD_2Cl_2 solution (0.017 mmol) in the same manner as described in the N_2O experiment (Figure

S14). ^1H NMR (400 MHz, CD_2Cl_2): δ 0.07 (s, $(\text{Me}_3\text{Si})_2\text{O}$), 0.43 (s, unreacted TMS-Cl), 1.31 (s, **1** Ar- CH_3), 1.39 (s, **1** Ar- CH_3), 2.15 (s, **1** Ar- CH_3), 2.17 (s, **1** Ar- CH_3), 2.69 (s, **1** Ar- CH_3), 2.77 (s, **1** Ar- CH_3), 3.63 (s, 18-crown-6), 6.10 (s, **1** NC(H)N), 6.25 (s, **1** Ar-CH), 6.31 (s, **1** Ar-CH), 6.61 (s, **1** NC(H)N), 6.71 (s, **1** Ar-CH).

Oxygen Trapping Experiment with Benzoyl Chloride. Inside a N_2 filled glovebox, to a Schlenk tube equipped with a Teflon screw cap and magnet stir bar, **2** (0.010 g, 0.0058 mmol) was added and dissolved in dichloromethane (5 mL). The tube was sealed with the Teflon cap and taken out of the glovebox and connected to Schlenk line streaming with N_2O . The solution in the flask was cooled to -78°C (dry ice and acetone bath) with stirring, and then opened to N_2O for 3 hours while maintaining the temperature at -78°C . Solvent was removed by vacuum evaporation and Schlenk tube was closed and pumped back into the glovebox. Purple evaporated residue inside Schlenk tube was mixed with approximately 8 mL of diethyl ether and 20 μL of a 0.287 M solution of cold (-32°C) benzoyl chloride (0.0057 mmol) in diethyl ether was added. Contents stirred for 1 hour at room temperature, pipette-filtered through Celite and solvent was removed by vacuum evaporation. Resulting residue was dissolved in C_6D_6 and pipette-filtered through Celite into an NMR tube for analysis (Figure S15-S16). ^1H NMR (400 MHz, C_6D_6): δ 1.46 (s, **1** Ar- CH_3), 1.57 (s, **1** Ar- CH_3), 2.18 (s, **1** Ar- CH_3), 2.20 (s, **1** Ar- CH_3), 2.83 (s, **1** Ar- CH_3), 2.97 (s, **1** Ar- CH_3), 3.52 (s, 18-crown-6), 6.37 (s, **1** Ar-CH), 6.44 (s, **1** Ar-CH), 6.94 (m, benzoic anhydride Ar-CH), 7.07 (m, benzoic anhydride Ar-CH), 7.96 (m, benzoic anhydride Ar-CH).

Reaction Headspace Analysis of $^{15}\text{N}_2$ Produced from the Reaction between $^{15}\text{N}_2\text{O}$ and **2.** Inside a N_2 filled glovebox, to a 100 mL round bottom Schlenk flask with a magnetic stir bar, **2** (0.125 g, 0.0732 mmol) was added and dissolved in THF (60 mL). The flask was sealed with a fresh septum secured with copper wire and a Keck clip. The flask was taken out of the glovebox

and connected to a T-shaped stopcock connected to a Schlenk line streaming both N₂ and ¹⁵N₂O gases. After five freeze-pump-thaw cycles, the flask was cooled to - 78° C (dry ice and acetone bath) and headspace was backfilled quickly with ¹⁵N₂O (~3 seconds) and then the flask was closed. The reaction was stirred at - 78° C for three hours, and then the cooling bath was removed. The reaction was then stirred for 3 hours at room temperature to equilibrate the gases in the reaction headspace and dissolved in the solution. The gases in the reaction headspace were then analyzed by 5 μL injections into GC-MS (Figure S21). After the 6 hour GC-MS headspace measurement, the reaction flask sat for 48 hours at room temperature, without stirring to prevent high pressure build-up within the flask. After 48 hours, the gases in the headspace were again analyzed by 5 μL injections into the GC-MS (Figures S17 and S19). To serve as a blank, a 50 mL round bottom Schlenk flask was sealed using a fresh septum secured with copper wire and a Keck clip. The blank flask was evacuated by vacuum and refilled with ¹⁵N₂O and then closed. Gases in blank flask were analyzed by a 5 μL injection (Figure S22). Blank flask then sat alongside the reaction flask for 48 hours at room temperature and was re-analyzed by GC-MS (Figure S18 and S20).

Computational Methods. All calculations were performed using Gaussian09, Revision B.01.⁶ Density functional theory (DFT) calculations were carried out using the B3LYP functional.⁷ Mixed basis sets were employed: the LANL2TZ(f) triple- ζ basis set⁸ with effective core potential⁹ was used for Cu, the Gaussian09 internal 6-311+G(d) basis set was used for S, and the Gaussian09 internal 6-31+G(d) basis set was used for C, H, and N. All calculations included a polarizable continuum model for dichloromethane solvation.¹⁰ The optimized coordinates for model **1'** (where the mesityl groups of **1** were replaced with methyls) at a slightly different level of theory were reported previously⁴ and were used as the starting point for obtaining optimized coordinates for neutral **1'** and anion **2'** (where the mesityl groups of **2** were replaced with methyls). Optimized

coordinates for both structures are enclosed below (Tables S2 and S3), along with comparisons of **1'** and **2'** to the experimental structures of **1** and **2** (Table S1). These optimized coordinates were used for single-point TD-DFT calculations (35 states for **1'**, 25 states for **2'**) at the same level of theory (see Figures S18-19). Lists of these transitions are included as Tables S4 and S5 below. Natural transition orbital analysis¹¹ was used to examine the nature of the dominant transition (State 9, 578 nm, 6000 M⁻¹cm⁻¹) in the predicted electronic spectrum of **2'**. The broken-symmetry S=0 and S=1 states of **1'** were found to be higher energy than the closed-shell S=0 state presented here, although all three states were within ± 2 kcal/mol of each other, indicating that high-level calculations are in order to accurately model **1**. Orbital surfaces and Mulliken spin density were plotted using Gaussview 4.1¹² and are presented with isovalues indicated in figure captions.

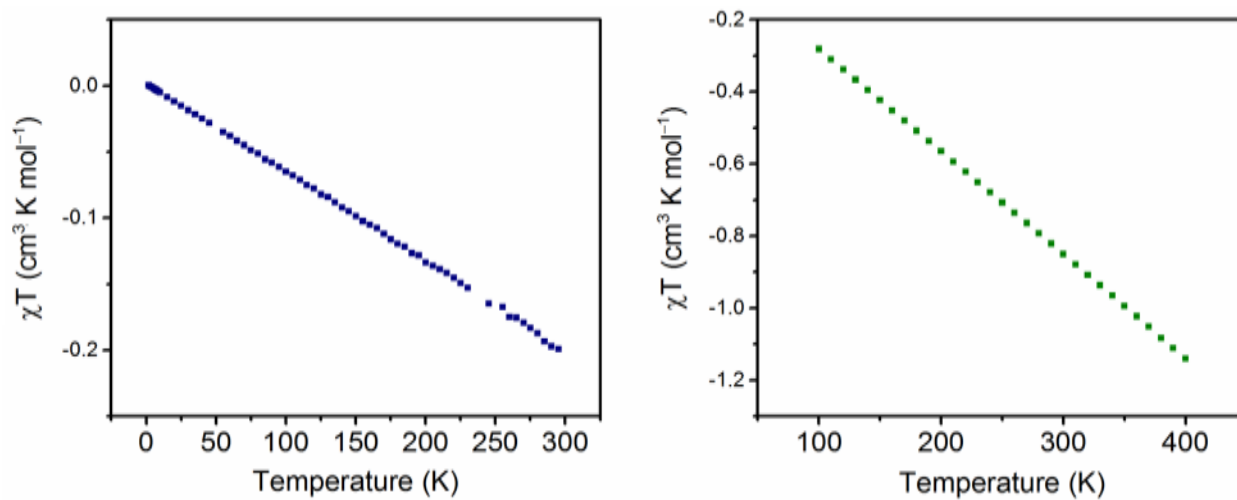


Figure S1. χT vs. temperature plots of **1**⁴ in a polyethylene bag at a field of 0.1 T (left) and a separate sample of **1** in a sealed quartz tube at a field of 7 T (right). Both depict a downward-sloping, linear curve, indicative of a diamagnetic sample. The significantly larger diamagnetic moment exhibited by the quartz-tube sample (right) is attributable to the additional mass of the quartz and eicosane.

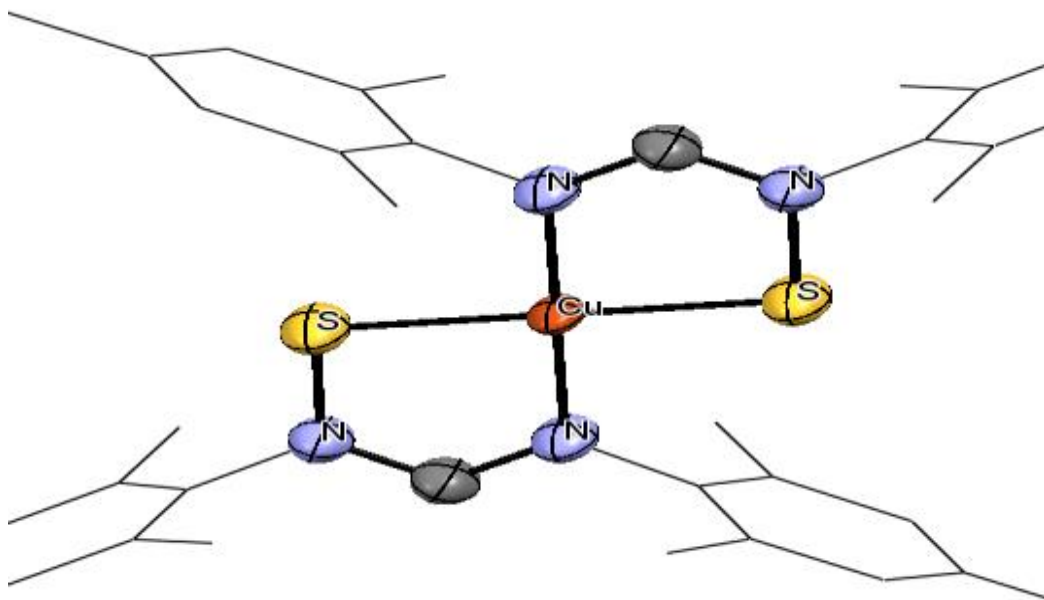


Figure S2. Solid state structure of Cu(II)S₂NCN₂ paramagnetic impurity determined by single-crystal X-ray diffraction. Mesityl groups are shown as wireframes and other atoms are displayed as 50% probability thermal ellipsoids. Hydrogen atoms have been omitted. Cu(II)S₂NCN₂ was isolated following the procedure published for **1**⁴ by S₈ with the following modifications: the reaction mixture was stirred for two days at r.t. The crude reaction solution was filtered through Celite and the filtrate was completely evaporated by vacuum. Recrystallization by vapor diffusion of the filtrate residue in CHCl₃ and pentane vapors leads to formation of maroon crystals.

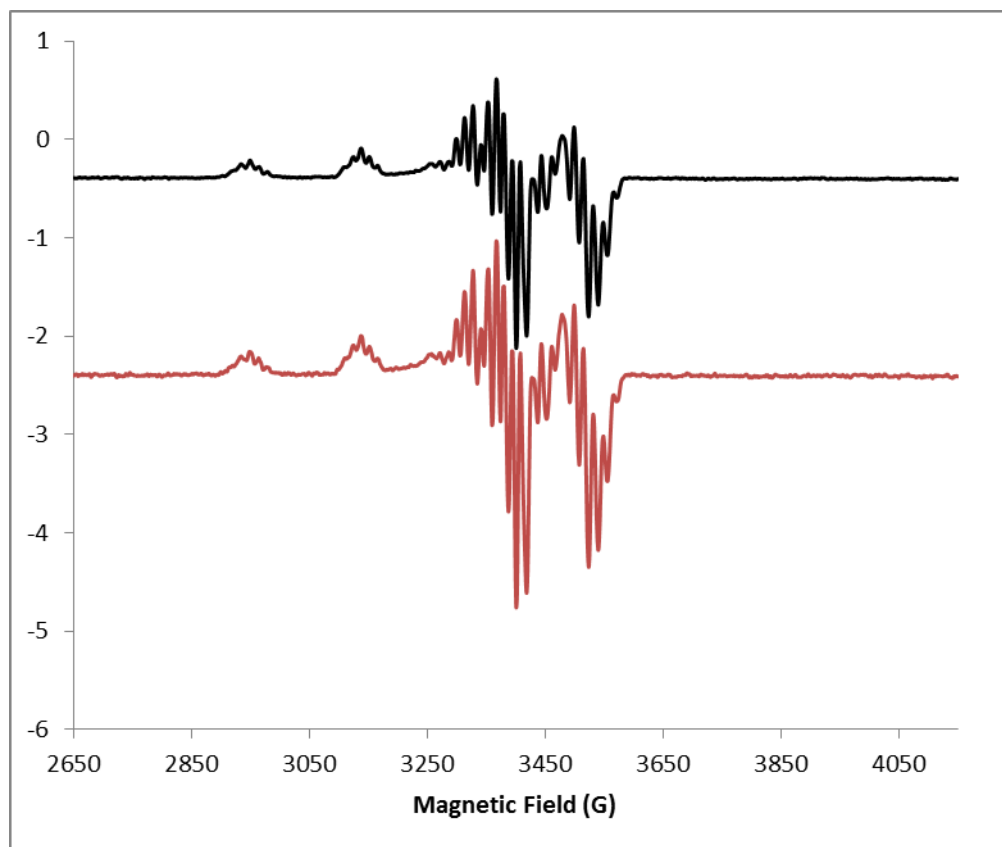


Figure S3. X-band EPR spectrum of the $\text{Cu(II)S}_2\text{NCN}_2$ species from Figure S2 at 34 K (black trace) and 24 K (red trace), power 46 dB.

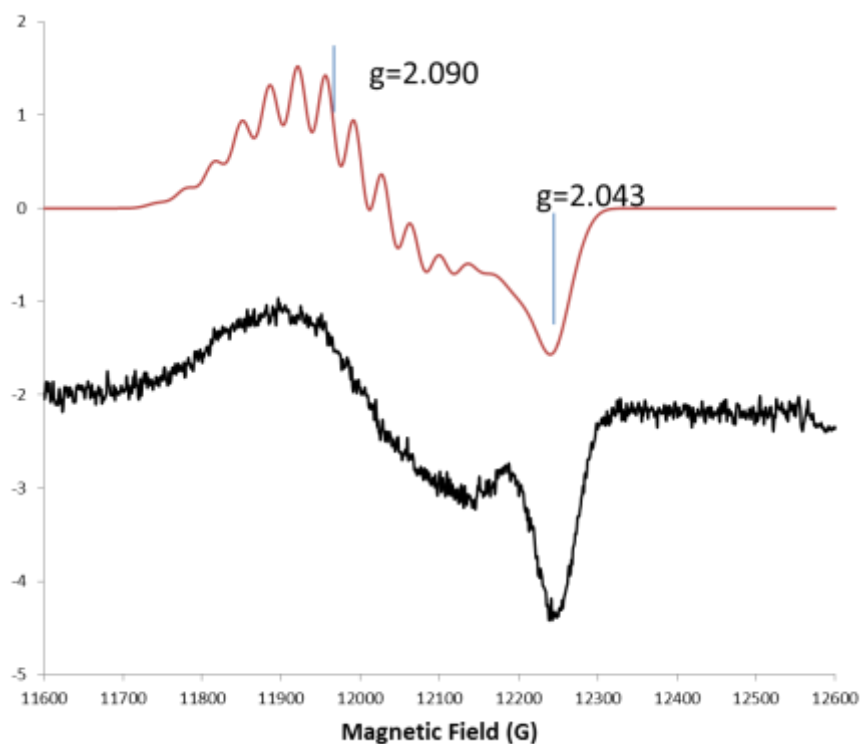


Figure S4. Q-band EPR spectrum for **2** (black scan): 34.99 GHz, -150 °C, 9 scans, power 22 dB, 10 G, mod.; time constant 0.1 sec; 2 min scans; Simulation (EasySpin, red scan): $g=2.09$, 2.043; four Cu's (both isotopes), $A=100$, 15 MHz; $lwpp=0.5$; $HStrain=100$ 90. $P_{1/2}$, the power for which the X-band EPR signal is one-half of the expected signal if unsaturated, is 22.5 dB at 10 K and 26.5 dB at 5 K. The spin-lattice relaxation time is faster for mixed valence complexes in both **2** and Cu_Z than for monomeric cupric complexes. The difference in the EPR spectra between **2** and Cu_Z is most easily seen in the Q-band spectrum, where $g \gg g_{||}$ for **2**, but $g \ll g_{||}$ for Cu_Z (P. Cheng...E.J. Solomon, J. Am. Chem. Soc., 124(5),744,2002) suggesting that the unpaired electron in **2** is not a pure dx^2-y^2 orbital. The line width for $g_{||}$ in the Q-band spectrum and simulations are used to approximate $A_{||}$. $A_{||}$ is obtained from resolved lines in the X-band spectrum and from simulations. Another difference between **2** and Cu_Z is that the spectra for **2** are simulated with four equivalent coppers and the spectra for Cu_Z are simulated with two sets of inequivalent coppers.

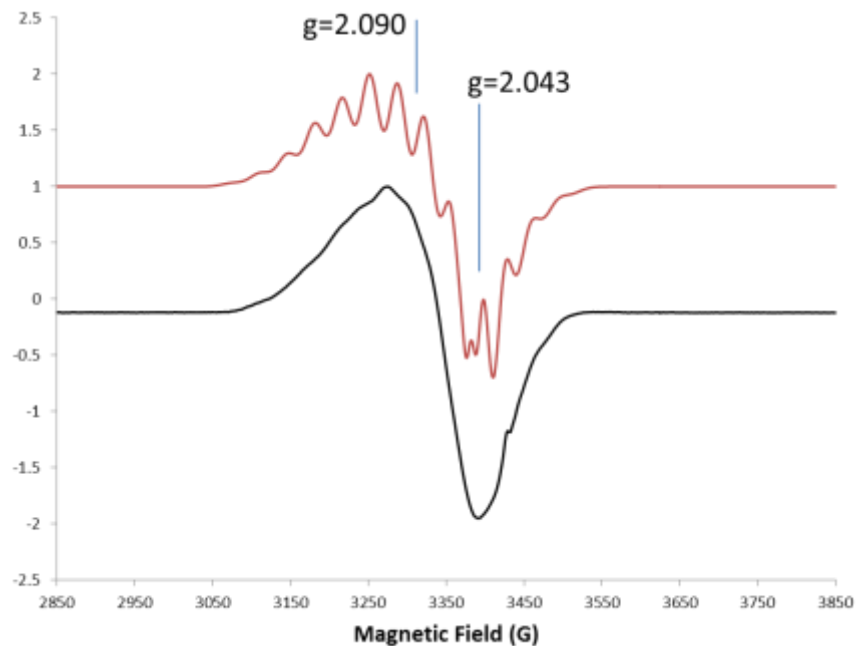


Figure S5. X-band EPR spectrum of **2** (black scan): 9.632 GHz, 9.9 K, 9 scans, power 46 dB; Simulation (red scan, EasySpin): $g = 2.09, 2.043$; both 63 and 65 isotopes, $A = 100, 15$ MHz, $lwpp=0.5$; $Hstrain:100\ 20$.

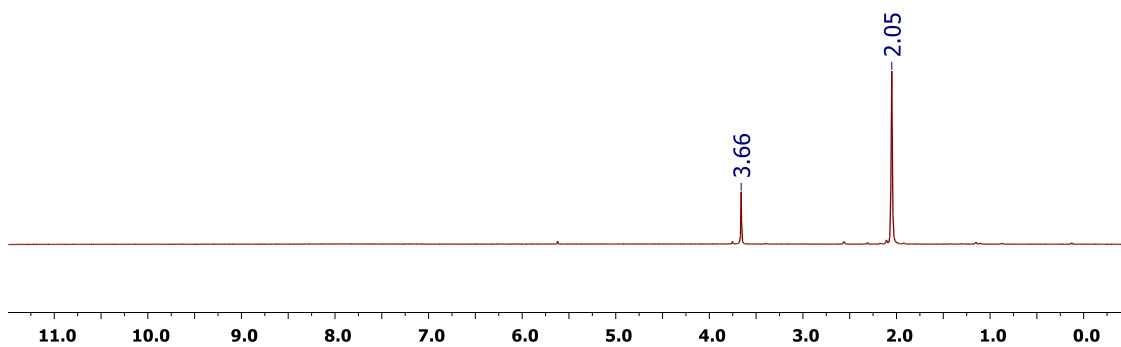


Figure S6. ^1H NMR (500 MHz) of **2** in Acetone- d_6 .

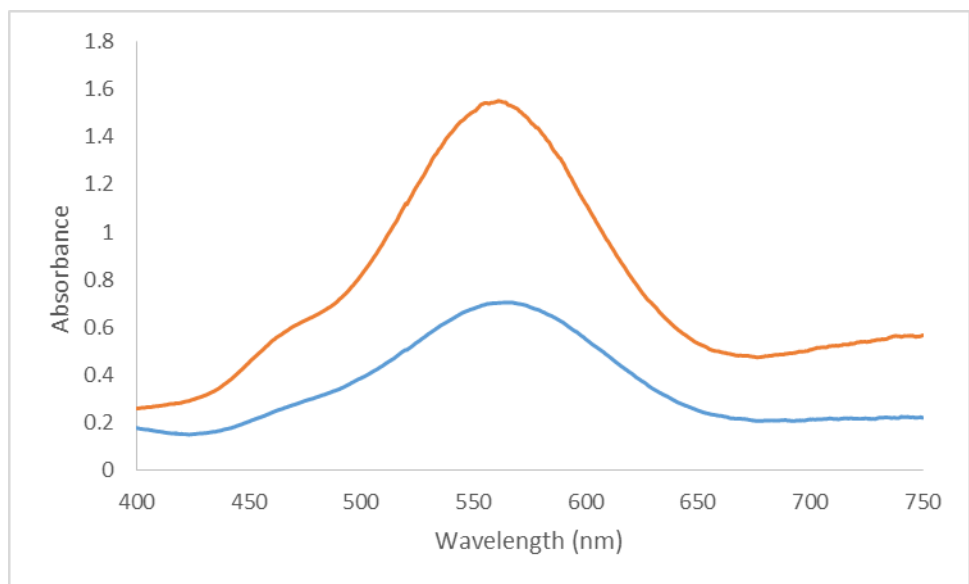


Figure S7. Absorption Spectra for 0.082 mM **2** (blue trace; absorption maxima at 565.5 nm; $\epsilon = 8601 \text{ M}^{-1}\cdot\text{cm}^{-1}$) and 0.085 mM **1**⁴ (orange trace; absorption maxima at 561 nm; $\epsilon = 18132 \text{ M}^{-1}\cdot\text{cm}^{-1}$) in THF at room temperature.

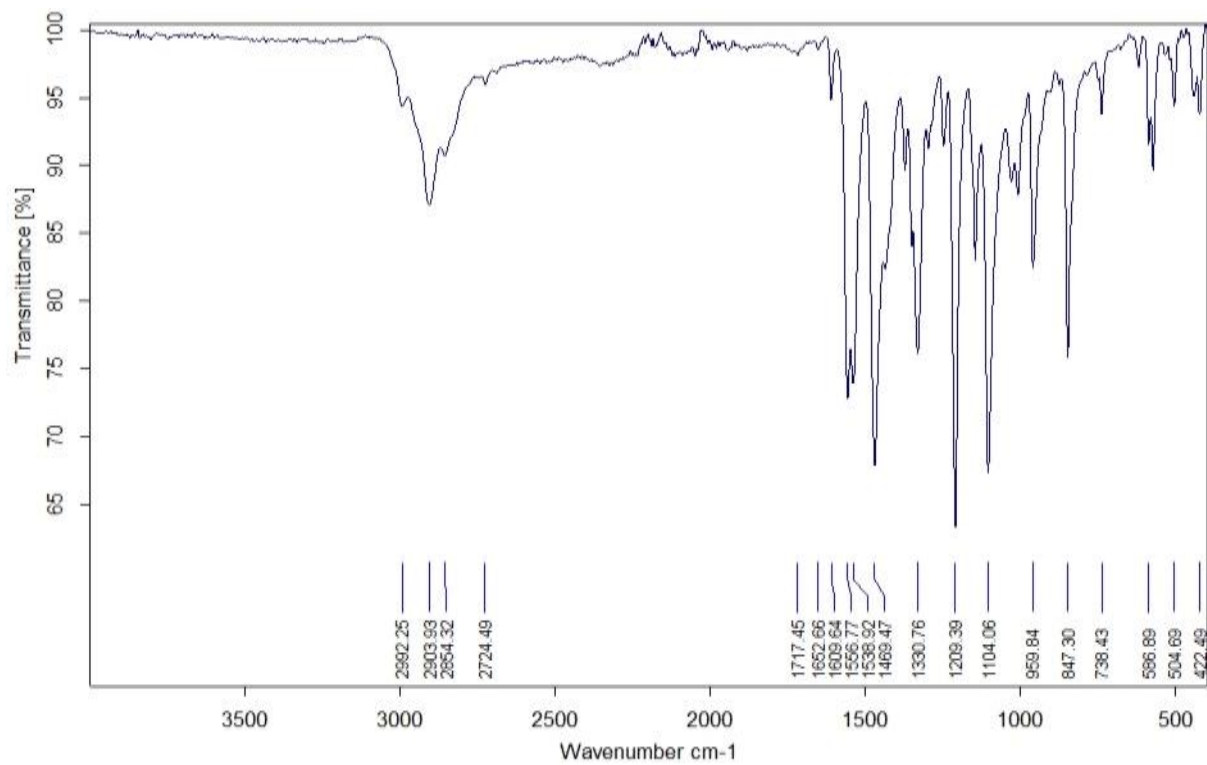


Figure S8. Infrared Spectrum of **2**.

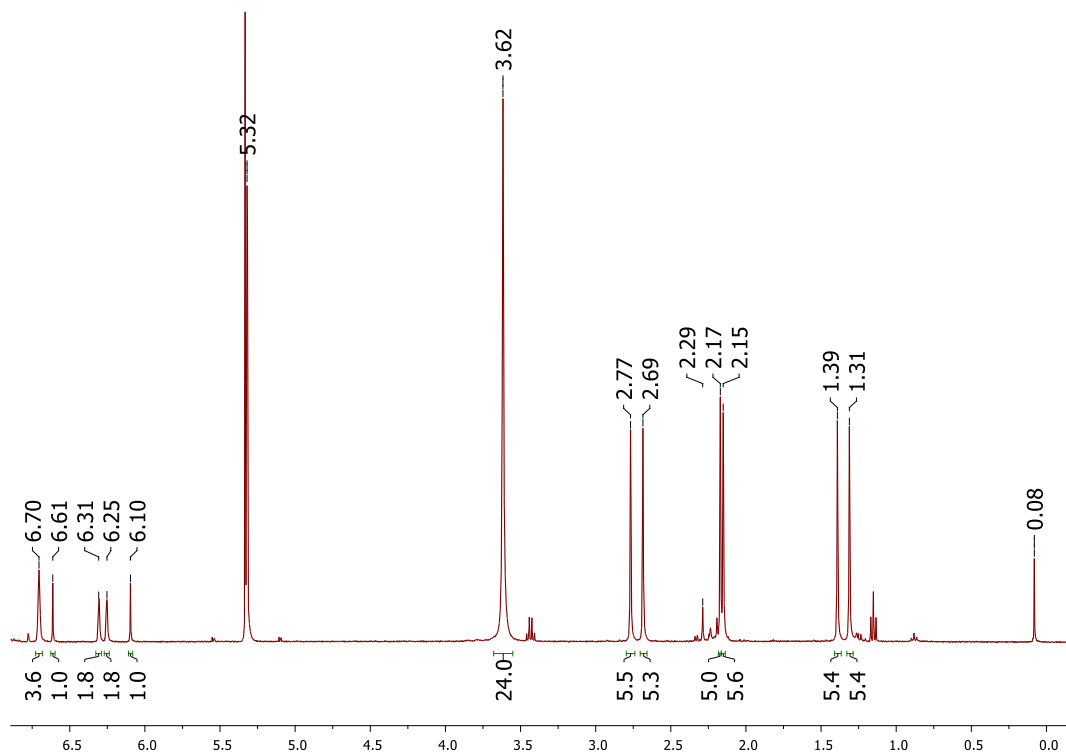


Figure S9. ^1H NMR (400 MHz, CD_2Cl_2) of reaction products from **2** + N_2O with appearance of **1** in 45% yield compared to integration of 18-crown-6 as the internal standard. Residual solvents in spectra are not peak picked. Peak appearing at 2.29 ppm is a decomposition product of **2**, $\text{Cu}_2[(2,4,6\text{-Me}_3\text{C}_6\text{H}_2\text{N})_2\text{C}(\text{H})]_2^4$.

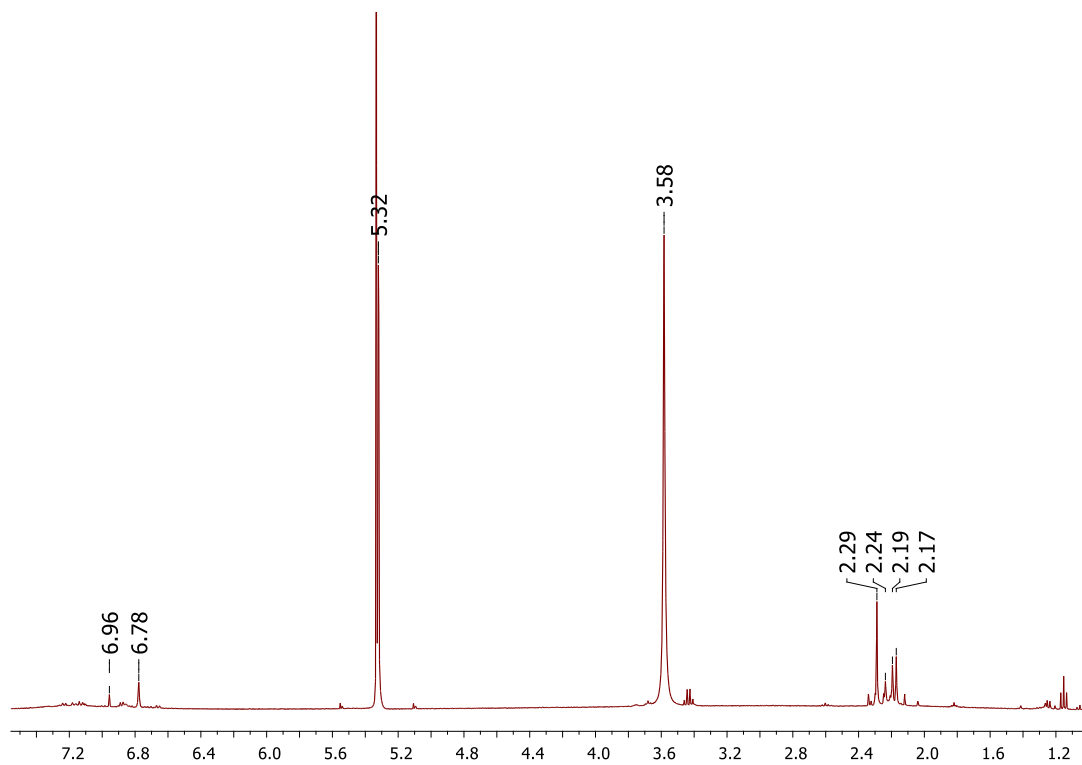


Figure S10. ¹H NMR (400 MHz, CD₂Cl₂) of control experiment between **2** and N₂. Residual solvents in spectra are not peak picked. Peaks appearing at 2.17- 2.29 ppm and 6.78- 6.96 ppm are decomposition products of **2**; Cu₂[(2,4,6-Me₃C₆H₂N)₂C(H)]₂⁴ and free ligand (bis(2,4,6-trimethylphenyl)formamidine)⁴. No presence of **1** is evident.

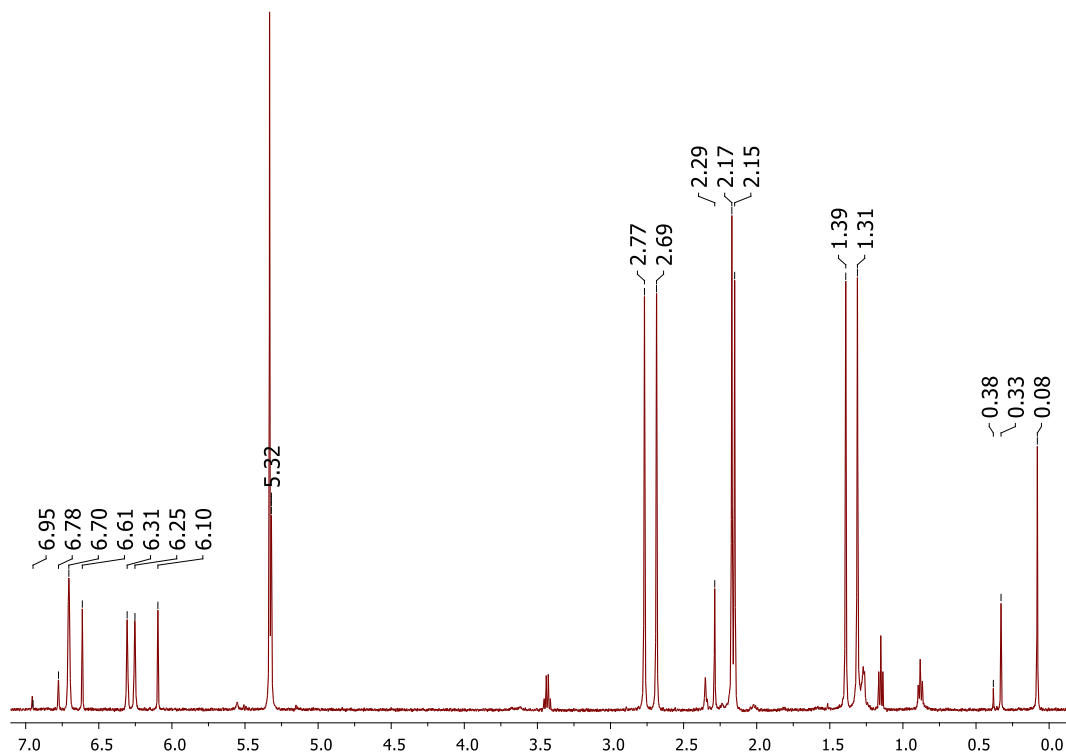


Figure S11. ^1H NMR (500 MHz, CD_2Cl_2) of **1** isolated after reaction between **2** and N_2O in CD_2Cl_2 (88% yield). Residual solvents in spectra are not peak picked. Peaks observed at 2.29, 6.78 and 6.95 ppm are the decomposition product of **2**, $\text{Cu}_2[(2,4,6\text{-Me}_3\text{C}_6\text{H}_2\text{N})_2\text{C}(\text{H})]_2^4$.

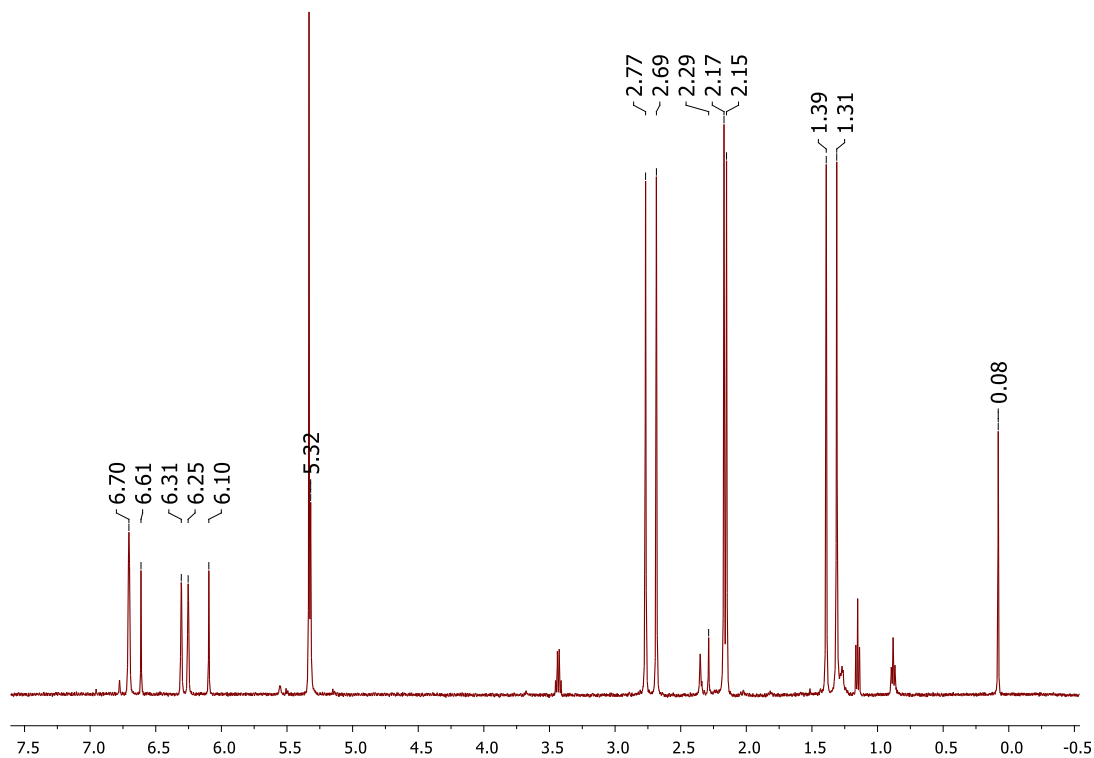


Figure S12. ^1H NMR (500 MHz, CD_2Cl_2) of **1** recovered after control experiment between **2** and N_2 (30% decomposition). Residual solvents in spectra are not peak picked. Peak observed at 2.29 ppm is the decomposition product of **2**, $\text{Cu}_2[(2,4,6\text{-Me}_3\text{C}_6\text{H}_2\text{N})_2\text{C}(\text{H})_2]^4$.

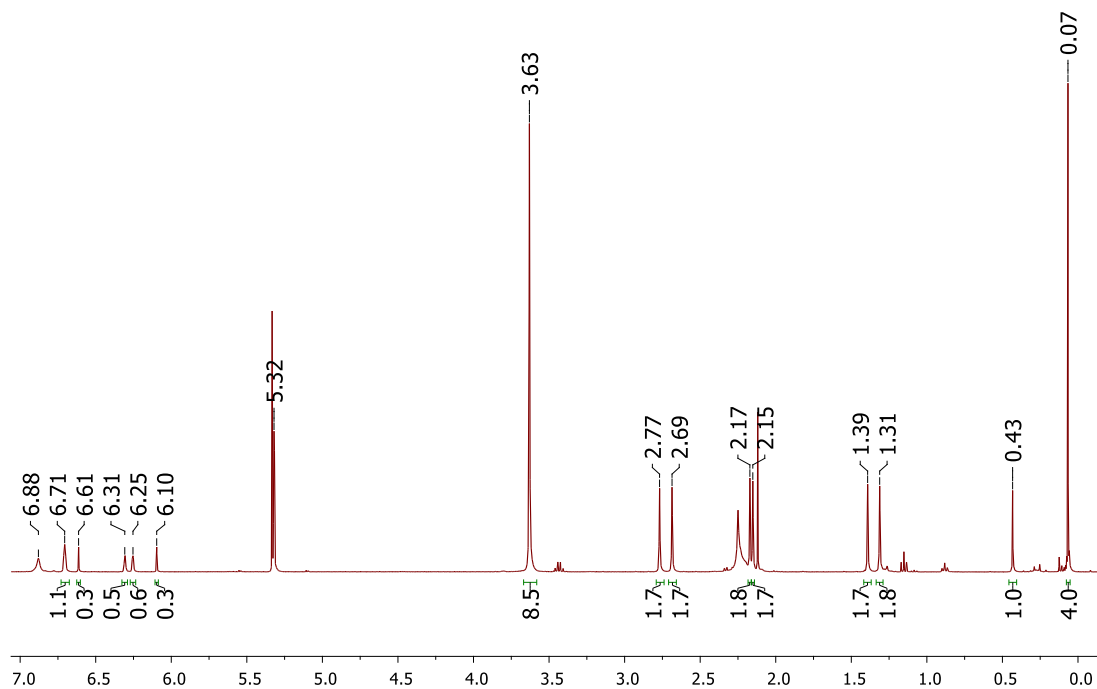


Figure S13. ¹H NMR (400 MHz, CD₂Cl₂) of reaction products from **2** + N₂O, using 5 equivalents of TMS-Cl as an oxygen trap. Hexamethyldisiloxane appearing at 0.07 ppm is the major product and some unreacted TMS-Cl appears at 0.43 ppm. Residual solvents in spectra are not peak picked.

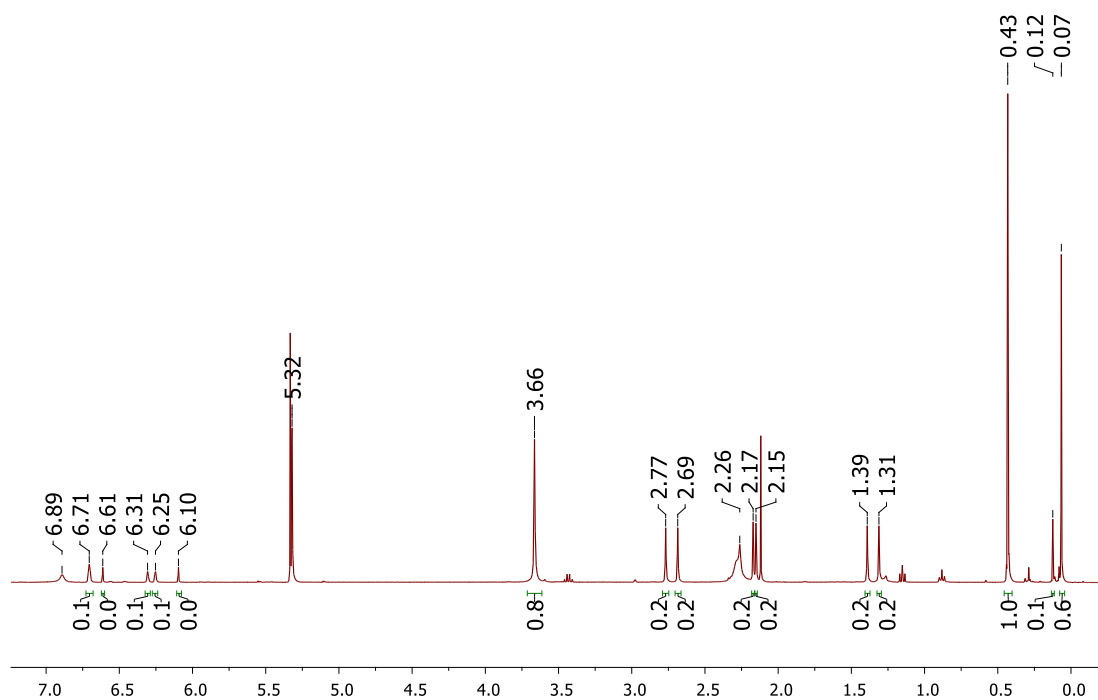


Figure S14. ¹H NMR (400 MHz, CD₂Cl₂) of resulting control experiment between **2** and N₂ and 5 equivalents of TMS-Cl. Residual solvents in spectra are not peak picked.

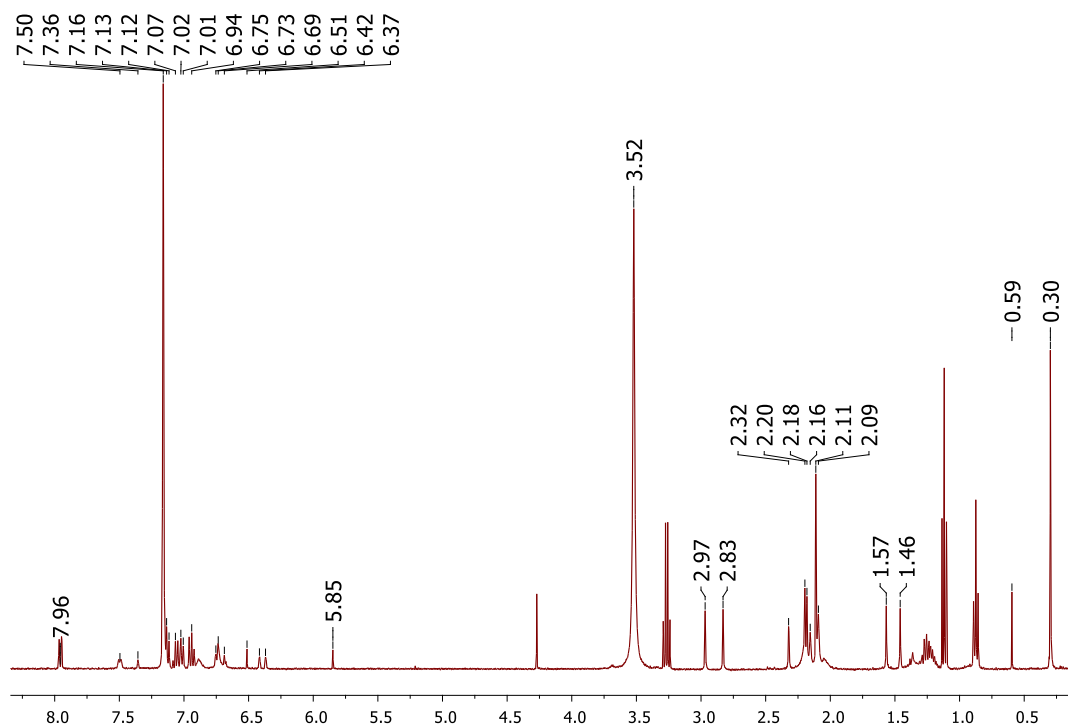


Figure S15. ^1H NMR (400 MHz, C_6D_6) of reaction products from **2** + N_2O using benzoyl chloride as an oxygen trap to form benzoic anhydride. Residual solvents in spectra are not peak picked.

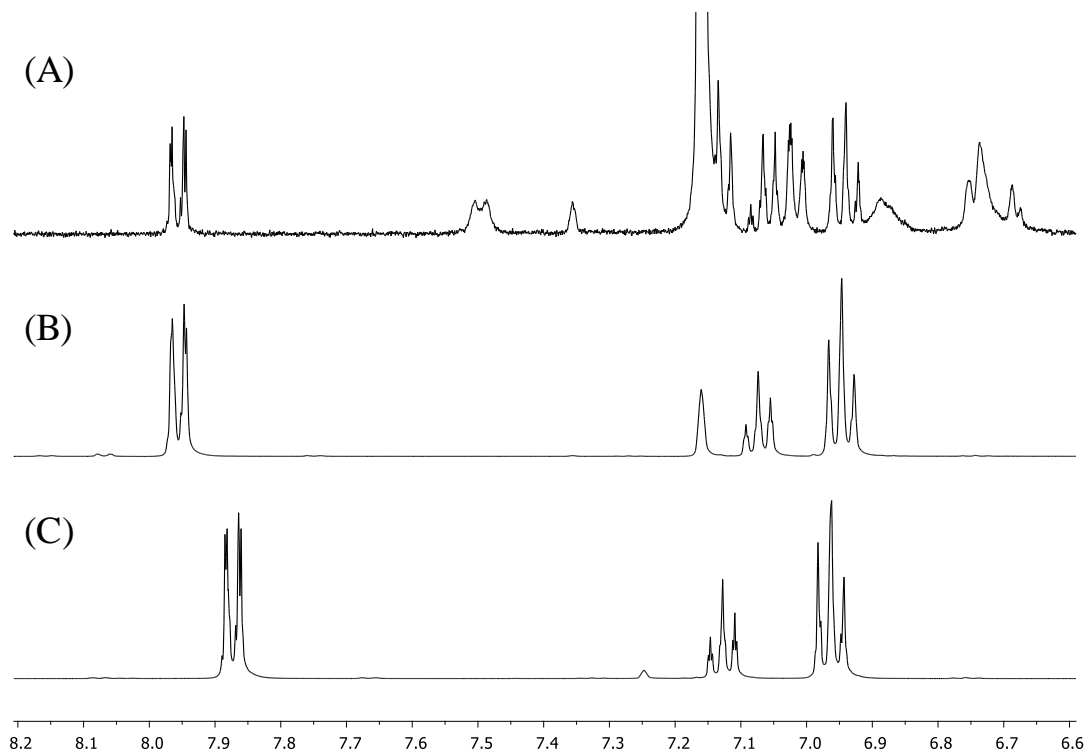


Figure S16. Comparison of ¹H NMR (400 MHz, C₆D₆) of reaction products from **2** + N₂O using benzoyl chloride as an oxygen trap to form benzoic anhydride (A); authentic sample of benzoic anhydride (B); authentic sample of benzoyl chloride (C).

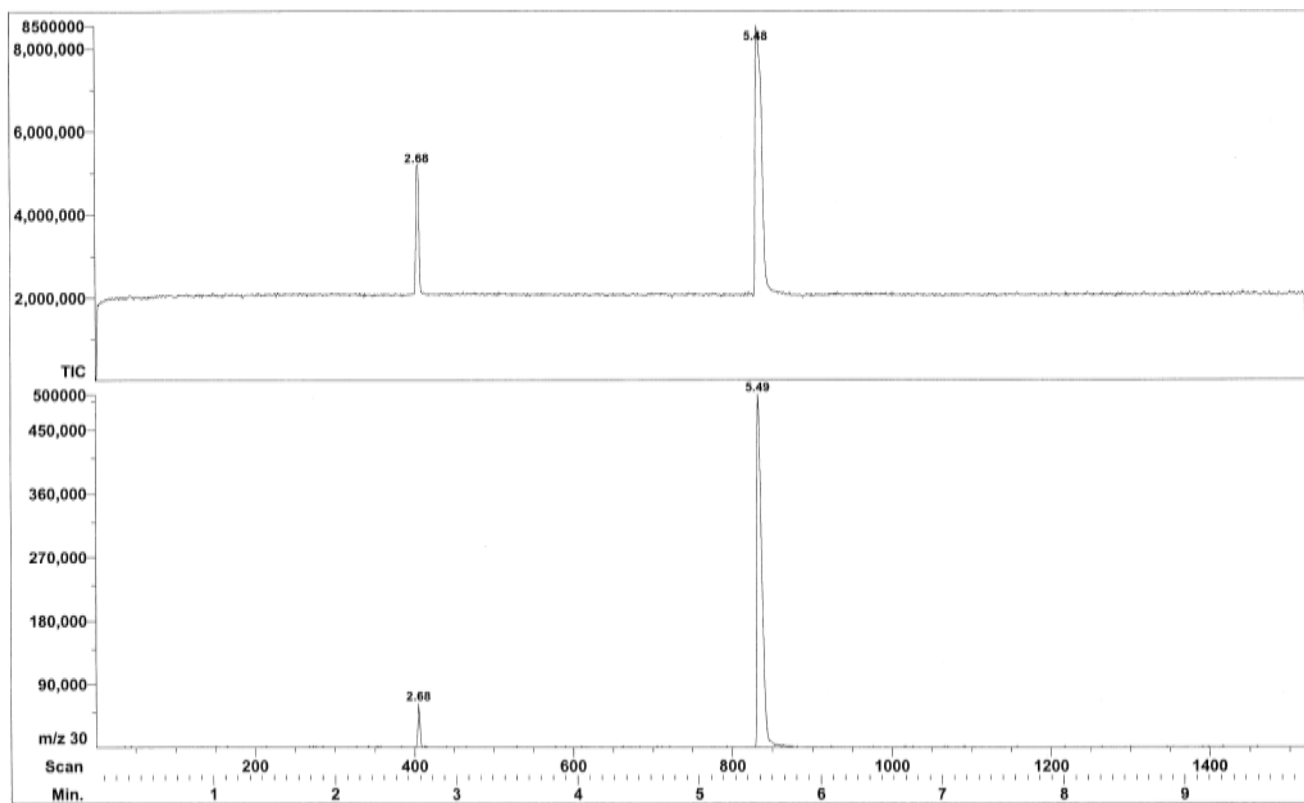


Figure S17. Total chromatogram (top) and extracted ion chromatogram for m/z 30 (bottom) from the reaction headspace after 48 hours of $^{15}\text{N}_2\text{O}$ and **2**.

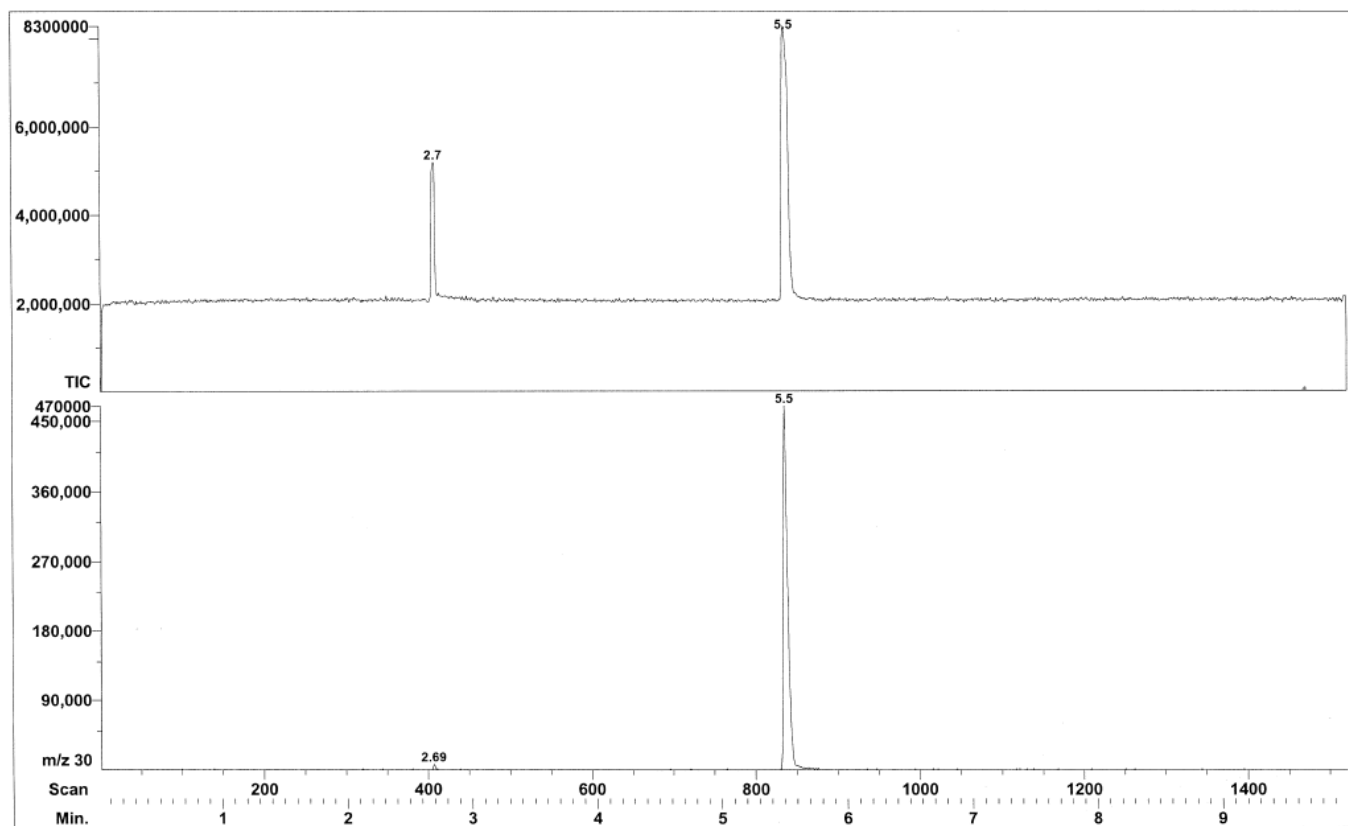


Figure S18. Total chromatogram (top) and extracted ion chromatogram for m/z 30 (bottom) from flask containing $^{15}\text{N}_2\text{O}$ for 48 hours.

Scan: 405 R.T.: 2.68
 Base: m/z 28; 100%FS #Ions: 28 TIC: 5173296 (Max Inten : 4193876)

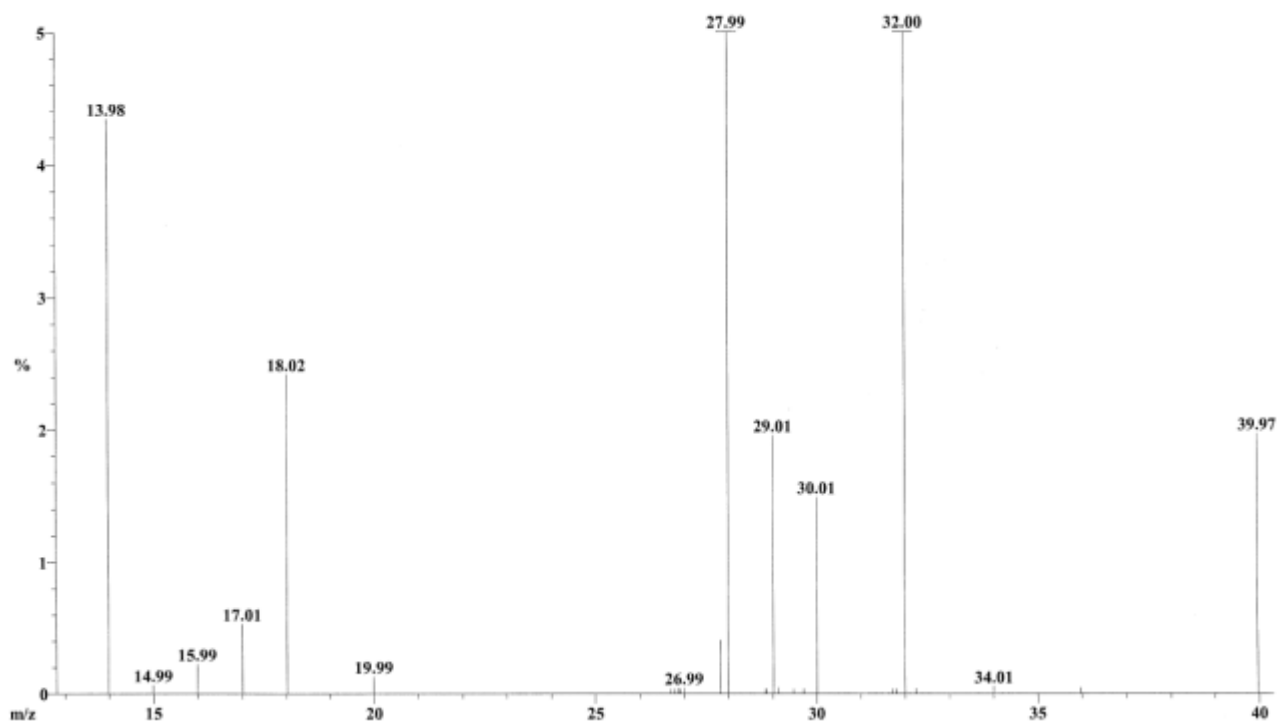


Figure S19. Mass spectrum of species at 2.68 minutes from the reaction headspace of $^{15}\text{N}_2\text{O}$ and **2** after 48 hours.

Table S1. Percent composition of species in Figure S19.

Scan: 405 R.T.: 2.68
 Base: m/z 28; 100%FS#Ions: 28 TIC: 5173296 (Max Inten : 4193876)

Threshold: .1% of Base

Displayed TIC: 5173296

Mass	%Base	%TIC	Intensity	Mass	%Base	%TIC	Intensity	Mass	%Base	%TIC	Intensity
13.9815	4.3	3.519	182,036	19.9908	.1	0.106	5,460	30.0124	1.5	1.209	62,548
15.9851	.2	0.182	9,428	27.8101	.4	0.328	16,980	31.9988	9.1	7.405	383,060
17.0069	.5	0.428	22,164	27.9929	100.0	81.068	4,193,876	39.9675	2.0	1.596	82,580
18.0212	2.4	1.961	101,460	29.0135	2.0	1.586	82,068				

Scan: 405 R.T.: 2.68
 Base: m/z 28; 58.7%FS #Ions: 18 TIC: 3112296 (Max Inten : 2461140)

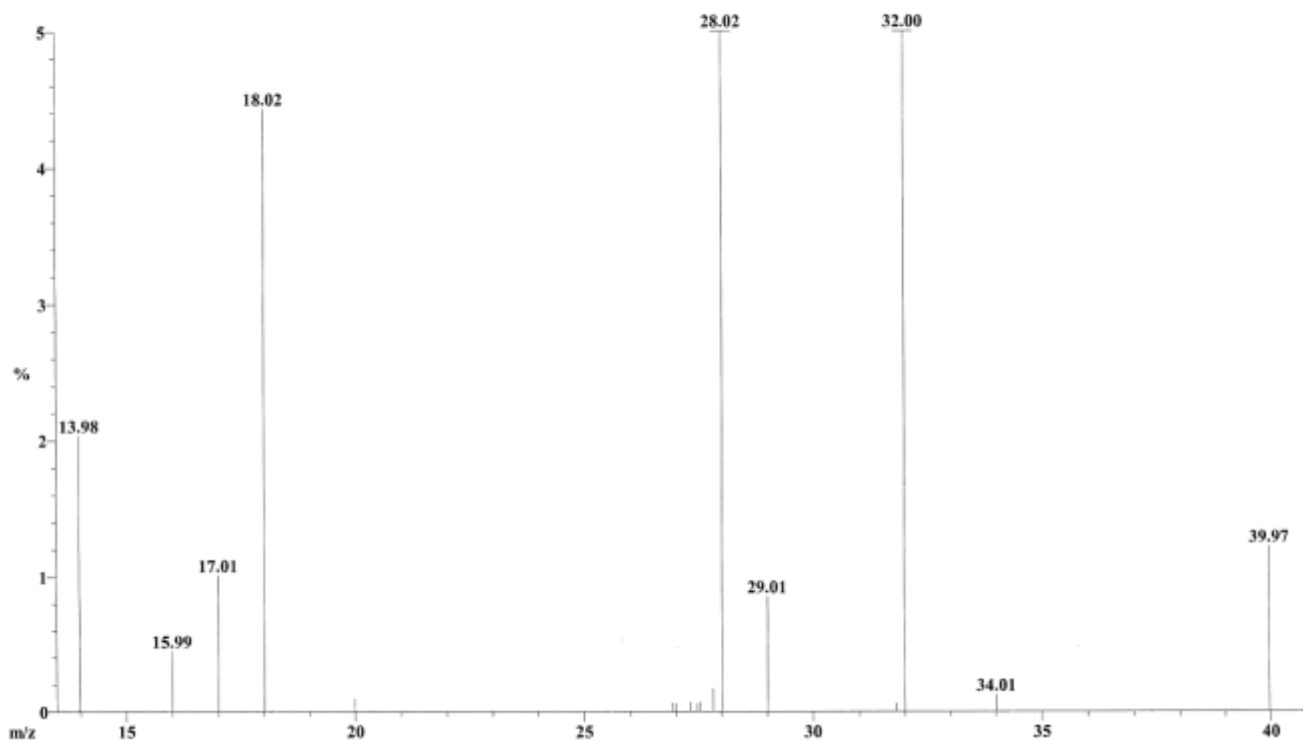


Figure S20. Mass spectrum of species at 2.68 minutes from a flask containing $^{15}\text{N}_2\text{O}$ after 48 hours.

Table S2. Percent composition of species in Figure S20.

Scan: 406 R.T.: 2.68
 Base: m/z 28; 100%FS#Ions: 26 TIC: 4968712 (Max Inten : 4193876)

Threshold: .1% of Base

Displayed TIC: 4968712

Mass	%Base	%TIC	Intensity	Mass	%Base	%TIC	Intensity	Mass	%Base	%TIC	Intensity
13.9815	2.9	2.468	122,644	18.0212	2.5	2.132	105,940	29.0135	1.1	0.965	47,956
15.9924	.2	0.195	9,684	27.8293	.2	0.196	9,748	31.9988	9.2	7.794	387,284
17.0069	.5	0.432	21,460	28.0121	100.0	84.406	4,193,876	39.9790	.8	0.715	35,540

Scan: 406 R.T.: 2.68
 Base: m/z 28; 100%FS #Ions: 24 TIC: 5072672 (Max Inten : 4193876)

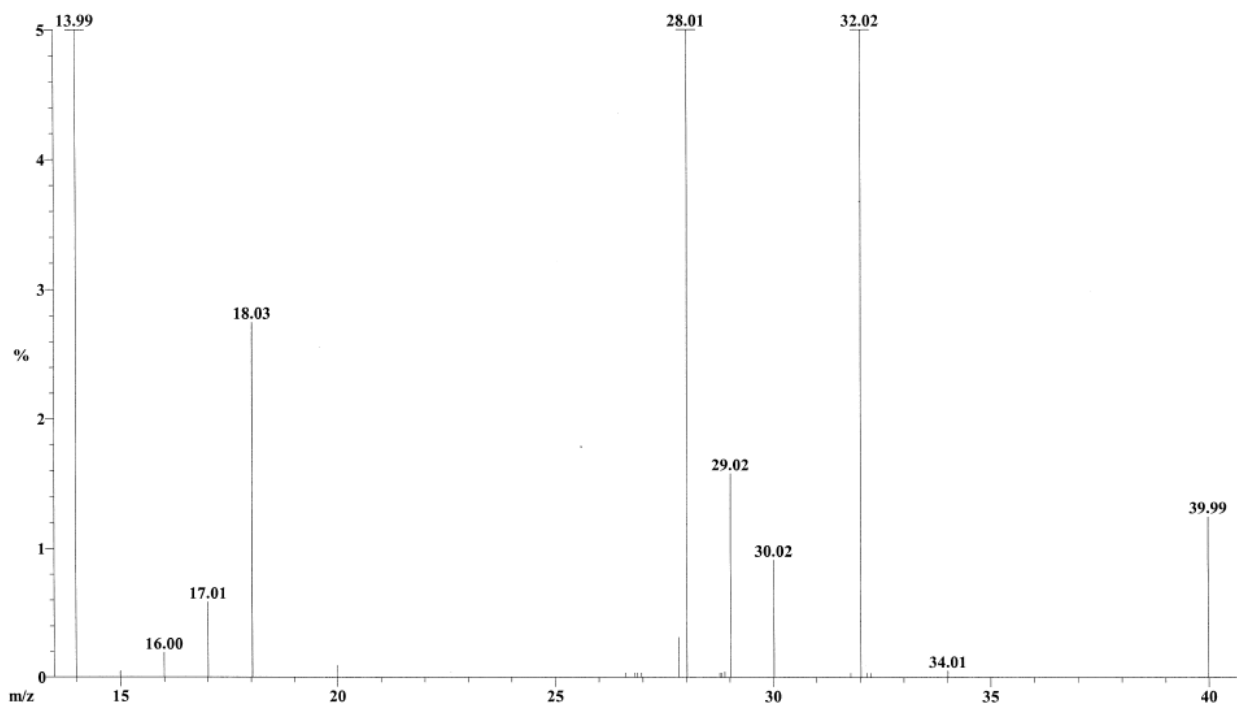


Figure S21. Mass spectrum of species at 2.68 minutes from the reaction headspace of $^{15}\text{N}_2\text{O}$ and **2** after 6 hours.

Table S3. Percent composition of species in Figure S21.

Scan: 406 R.T.: 2.68
 Base: m/z 28; 100%FS#Ions: 24 TIC: 5072672 (Max Inten : 4193876)

Threshold: .1% of Base

Displayed TIC: 5072672

Mass	%Base	%TIC	Intensity	Mass	%Base	%TIC	Intensity	Mass	%Base	%TIC	Intensity
13.9855	5.1	4.175	211,796	27.8257	.3	0.259	13,140	32.0156	7.7	6.338	321,492
15.9969	.2	0.158	8,020	28.0085	100.0	82.676	4,193,876	39.9904	1.3	1.034	52,436
17.0115	.6	0.484	24,532	29.0195	1.6	1.304	66,132				
18.0261	2.7	2.273	115,284	30.0185	.9	0.756	38,356				

Scan: 408 R.T.: 2.69
 Base: m/z 28; 93.2%FS #Ions: 21 TIC: 4576356 (Max Inten : 3907156)

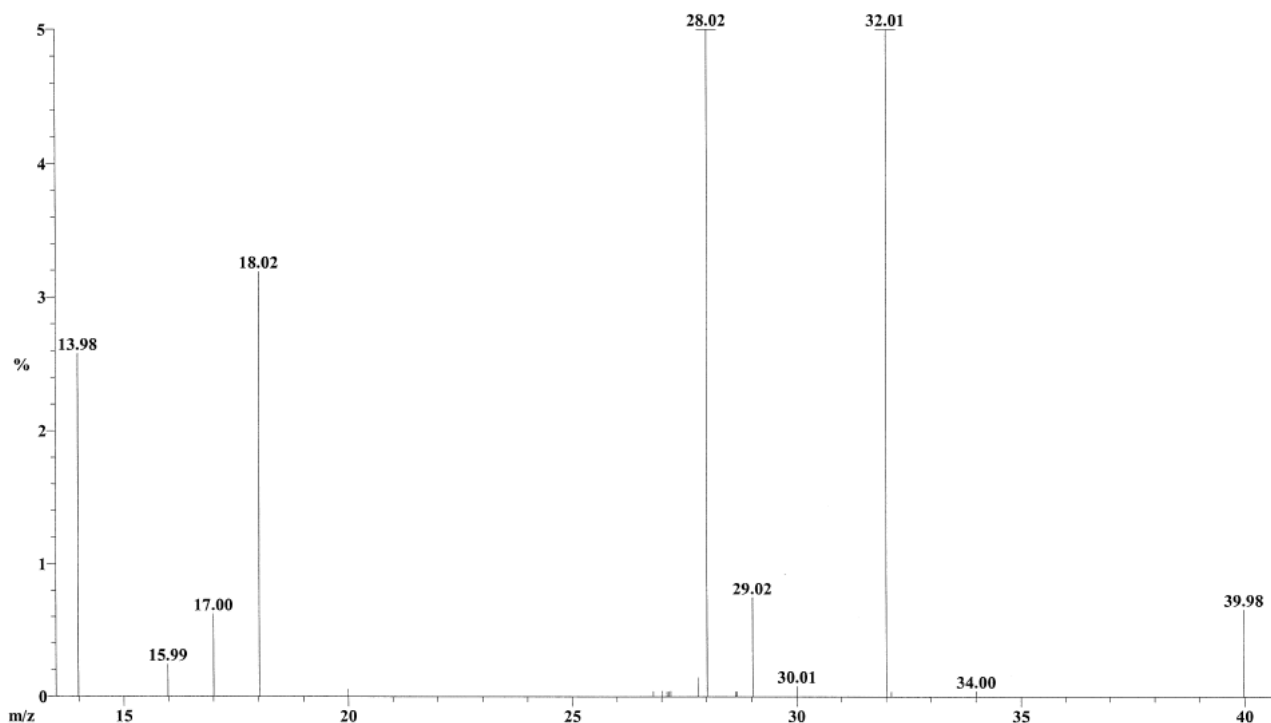


Figure S22. Mass spectrum of species at 2.69 minutes from flask containing $^{15}\text{N}_2\text{O}$.

Table S4. Percent composition of species in Figure S22.

Scan: 408 R.T.: 2.69
 Base: m/z 28; 93.2%FS#Ions: 21 TIC: 4576356 (Max Inten : 3907156)

Threshold: .1% of Base

Displayed TIC: 4576356

Mass	%Base	%TIC	Intensity	Mass	%Base	%TIC	Intensity	Mass	%Base	%TIC	Intensity
13.9786	2.6	2.200	100,692	18.0183	3.2	2.722	124,564	29.0195	.7	0.638	29,204
15.9895	.2	0.206	9,428	27.8257	.1	0.125	5,716	32.0052	8.4	7.137	326,612
17.0040	.6	0.530	24,276	28.0181	100.0	85.377	3,907,156	39.9789	.7	0.561	25,684

Scan: 832 R.T.: 5.48
 Base: m/z 46; 100%FS #Ions: 40 TIC: 8115232 (Max Inten : 4193876)

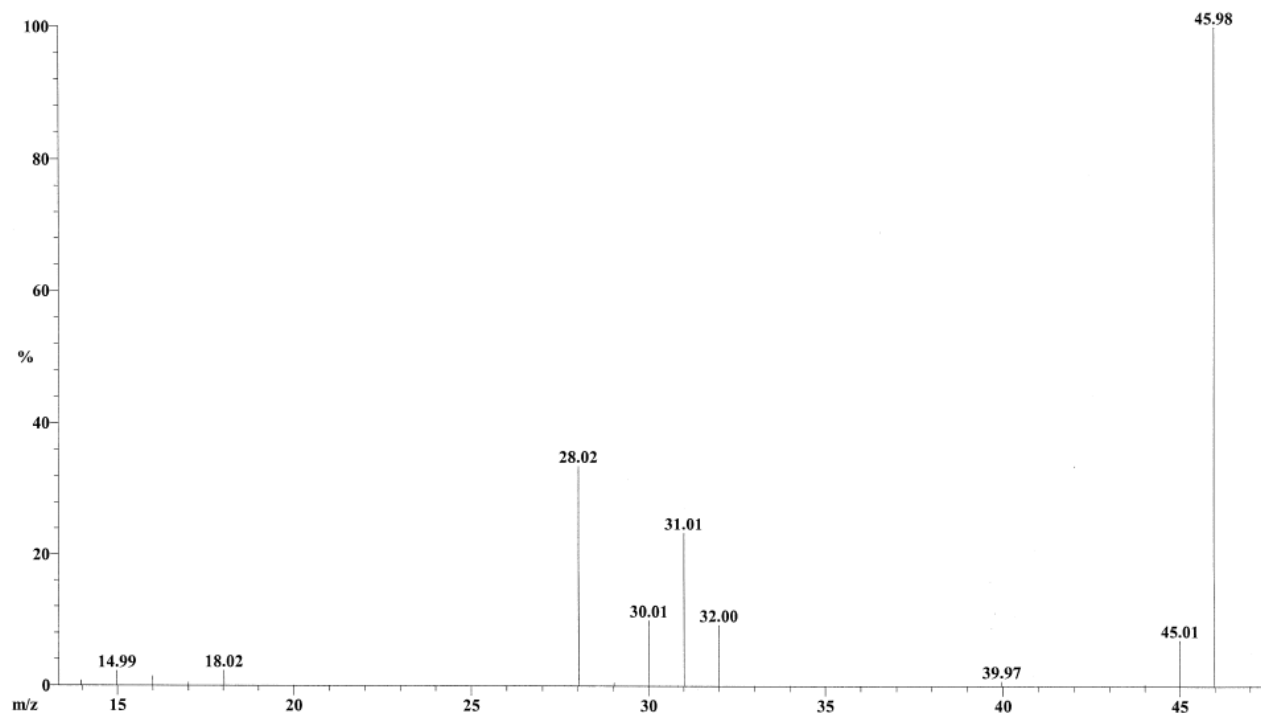


Figure S23. Mass spectrum of species at 5.48 minutes from the chromatogram of the reaction headspace of $^{15}\text{N}_2\text{O}$ and **2** in Figure S17.

Table S5. Summary integration values of $^{15}\text{N}_2$ from reaction headspace experiments with $^{15}\text{N}_2\text{O}$ and **2**, after 6 and 48 hours compared to the $^{15}\text{N}_2\text{O}$ blank. Integration values were obtained from the extracted ion chromatogram for m/z 30 for the peak with the retention time of 2.68 minutes (bottom of Figure S17 and Figure S18).

	Reaction $^{15}\text{N}_2$ Peak Integration	Blank $^{15}\text{N}_2$ Peak Integration
48 Hours	181,583	21,394
6 Hours	109,835	22,868

Table S6. Comparison of calculated and experimental bond distances (Å).

	1' (calculated)	1 (experimental)	2' (calculated)	2 (experimental)
Cu1-Cu2	2.469	2.4226(6)	2.584	2.502(1), 2.486(1)
Cu2-Cu3	2.928	3.0353(6)	2.827	2.809(1), 2.854(1)
Cu3-Cu4	2.469	2.4226(6)	2.584	2.532(1), 2.500(1)
Cu1-Cu4	2.928	3.0353(6)	2.827	2.831(1), 2.844(1)
Average Cu-S	2.261	2.180	2.302	2.217

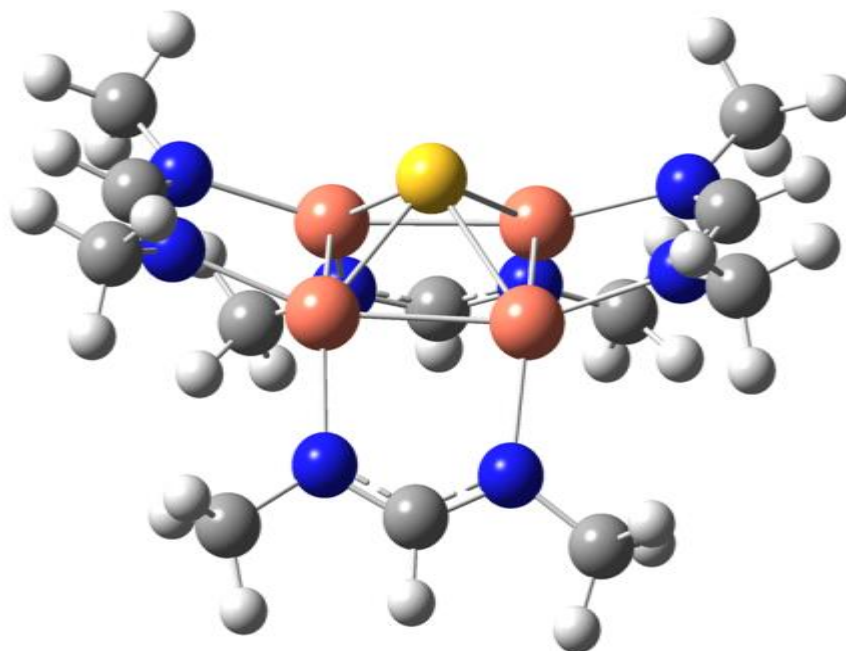


Figure S24. Optimized structure of 2'.

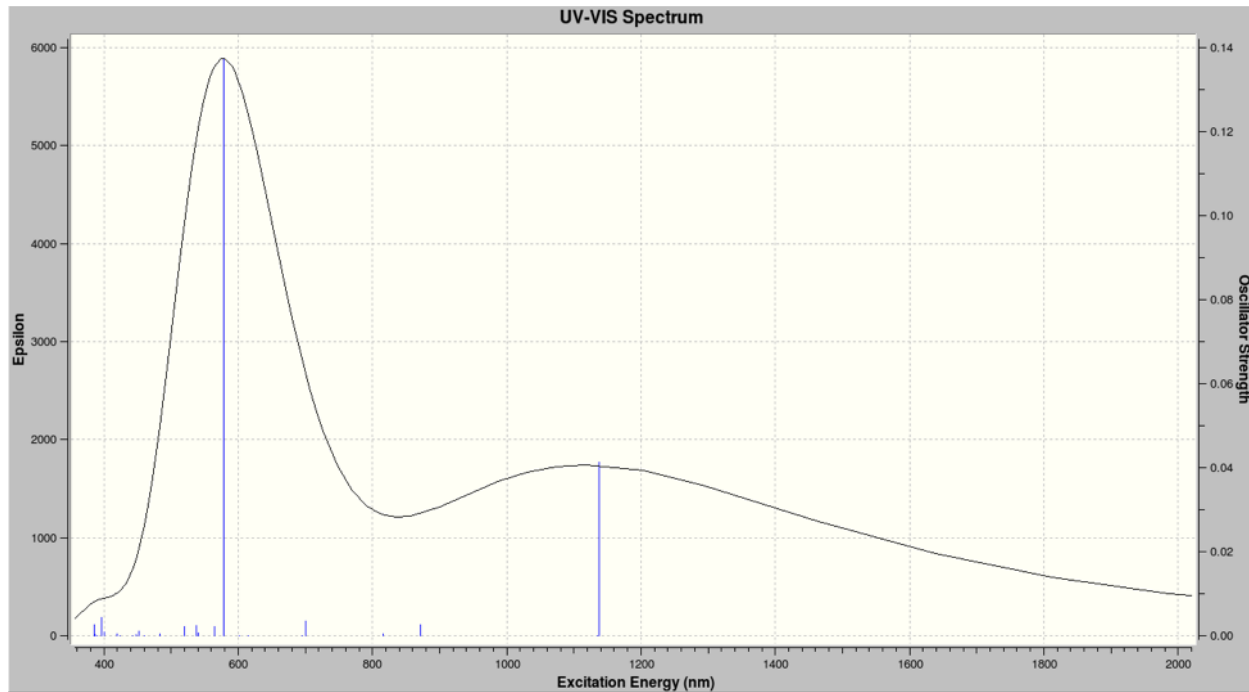


Figure S25. Calculated UV-Vis spectrum of 2'.

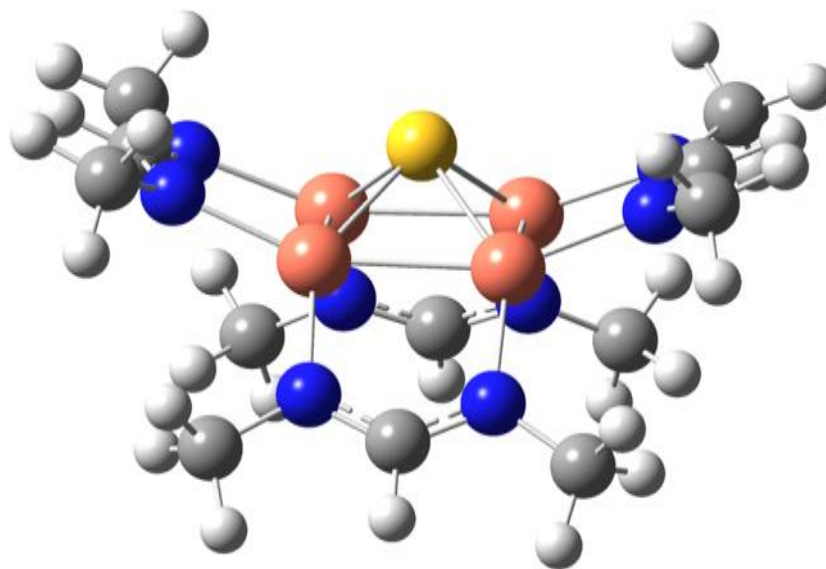


Figure S26. Optimized structure of 1'.

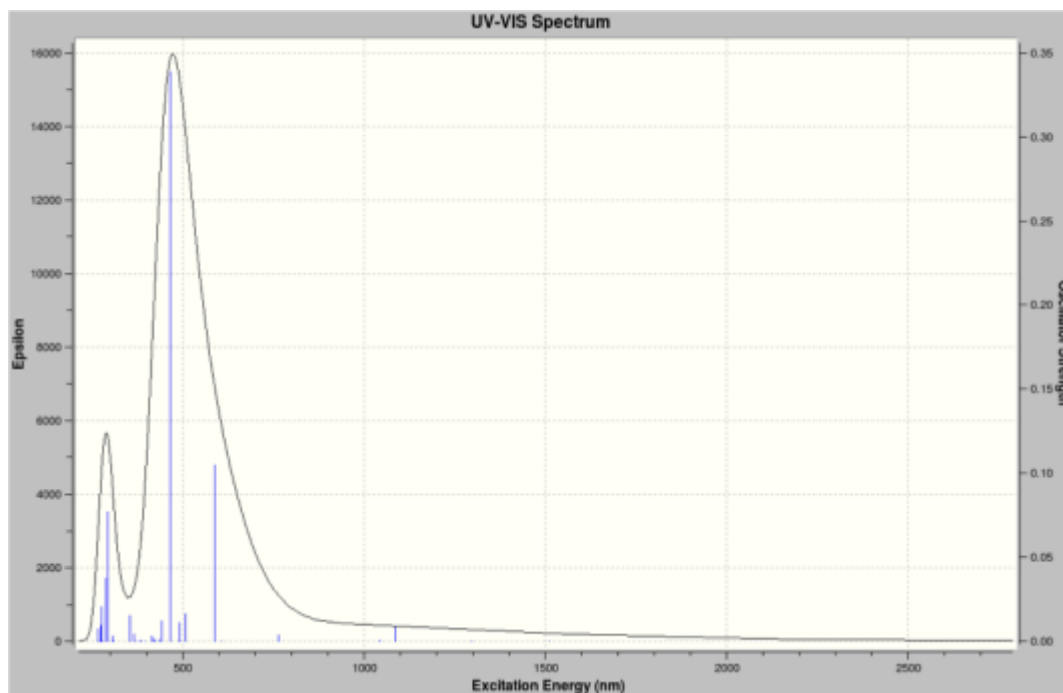


Figure S27. Calculated UV-Vis spectrum of 1'.

Table S7. Optimized coordinates of **2'**.

Center	Atomic	Atomic	Coordinates (Angstroms)			
Number	Number	Type	X	Y	Z	

1	29	0	1.386449	-1.349982	-0.224024	
2	16	0	0.000002	-0.000076	-1.474806	
3	7	0	3.281351	-0.976101	-0.923119	
4	7	0	3.126323	1.380414	-0.861635	
5	6	0	3.733485	0.243940	-1.159060	
6	1	0	4.723098	0.321561	-1.645214	
7	29	0	-1.386447	1.349952	-0.224154	
8	7	0	-3.281346	0.976012	-0.923222	
9	7	0	-3.126316	-1.380499	-0.861544	
10	6	0	-3.733473	-0.244049	-1.159074	
11	1	0	-4.723075	-0.321712	-1.645242	
12	29	0	-1.194111	-1.470350	-0.169276	
13	7	0	-0.983854	-2.734209	1.363758	
14	7	0	1.364907	-2.687537	1.258960	
15	6	0	0.218929	-3.082077	1.789964	
16	1	0	0.271111	-3.754926	2.662529	
17	29	0	1.194104	1.470329	-0.169420	
18	7	0	0.983846	2.734363	1.363467	
19	7	0	-1.364915	2.687653	1.258698	
20	6	0	-0.218937	3.082258	1.789654	
21	1	0	-0.271117	3.755185	2.662158	
22	6	0	-4.104976	2.086128	-1.378376	
23	1	0	-4.335943	2.772439	-0.551923	

24	1	0	-3.588327	2.676106	-2.150727
25	1	0	-5.062706	1.748165	-1.807901
26	6	0	-3.808144	-2.611006	-1.234625
27	1	0	-4.788424	-2.420762	-1.702280
28	1	0	-3.210188	-3.195840	-1.949527
29	1	0	-3.978270	-3.252732	-0.358617
30	6	0	-2.127197	-3.266063	2.093188
31	1	0	-2.789334	-2.456198	2.427473
32	1	0	-2.728135	-3.934564	1.460693
33	1	0	-1.820489	-3.837150	2.983909
34	6	0	2.587763	-3.192080	1.869003
35	1	0	3.264894	-2.367038	2.125869
36	1	0	2.386510	-3.760642	2.791011
37	1	0	3.133163	-3.856012	1.182523
38	6	0	4.104985	-2.086257	-1.378171
39	1	0	5.062724	-1.748332	-1.807706
40	1	0	4.335933	-2.772504	-0.551660
41	1	0	3.588346	-2.676293	-2.150485
42	6	0	3.808163	2.610891	-1.234795
43	1	0	3.978266	3.252684	-0.358834
44	1	0	4.788454	2.420608	-1.702409
45	1	0	3.210227	3.195670	-1.949759
46	6	0	2.127192	3.266324	2.092813
47	1	0	2.789424	2.456516	2.427042
48	1	0	2.728025	3.934883	1.460277
49	1	0	1.820497	3.837380	2.983559
50	6	0	-2.587772	3.192221	1.868715
51	1	0	-2.386519	3.760866	2.790672
52	1	0	-3.133196	3.856082	1.182186

53 1 0 -3.264882 2.367186 2.125659

Table S8. Optimized coordinates of **1'**.

Center Number	Atomic Number	Atomic Type	Coordinates (Angstroms)		
			X	Y	Z
1	29	0	1.309161	-1.408896	-0.176093
2	16	0	0.000030	-0.000018	-1.366232
3	7	0	3.123631	-1.031322	-0.923548
4	7	0	3.004493	1.333672	-0.894061
5	6	0	3.590064	0.180910	-1.162130
6	1	0	4.583731	0.236714	-1.629581
7	29	0	-1.309162	1.408912	-0.176201
8	7	0	-3.123593	1.031285	-0.923732
9	7	0	-3.004442	-1.333708	-0.894173
10	6	0	-3.590005	-0.180955	-1.162305
11	1	0	-4.583648	-0.236781	-1.629805
12	29	0	-1.157468	-1.514723	-0.152193
13	7	0	-1.027289	-2.830246	1.301666
14	7	0	1.317693	-2.747879	1.262167
15	6	0	0.167111	-3.191147	1.742215
16	1	0	0.206278	-3.905971	2.577536
17	29	0	1.157482	1.514715	-0.152169
18	7	0	1.027225	2.830266	1.301657
19	7	0	-1.317758	2.747935	1.262025
20	6	0	-0.167196	3.191189	1.742132

21	1	0	-0.206399	3.906025	2.577442
22	6	0	-3.927349	2.169324	-1.361351
23	1	0	-4.165283	2.829723	-0.518974
24	1	0	-3.385261	2.766474	-2.107040
25	1	0	-4.875848	1.848734	-1.815429
26	6	0	-3.693299	-2.557939	-1.292745
27	1	0	-4.671398	-2.346570	-1.747857
28	1	0	-3.098340	-3.120147	-2.025142
29	1	0	-3.859048	-3.212817	-0.429241
30	6	0	-2.193353	-3.416698	1.953617
31	1	0	-2.919871	-2.638329	2.215184
32	1	0	-2.700891	-4.136000	1.296463
33	1	0	-1.917232	-3.945138	2.877449
34	6	0	2.543713	-3.261118	1.863637
35	1	0	3.231249	-2.439063	2.094298
36	1	0	2.339983	-3.804238	2.797769
37	1	0	3.065933	-3.948915	1.184318
38	6	0	3.927278	-2.169374	-1.361332
39	1	0	4.875974	-1.848822	-1.815025
40	1	0	4.164834	-2.830094	-0.519102
41	1	0	3.385291	-2.766176	-2.107378
42	6	0	3.693513	2.557897	-1.292372
43	1	0	3.859656	3.212442	-0.428686
44	1	0	4.671436	2.346476	-1.747840
45	1	0	3.098468	3.120487	-2.024398
46	6	0	2.193256	3.416734	1.953655
47	1	0	1.917091	3.945163	2.877480
48	1	0	2.919775	2.638376	2.215245
49	1	0	2.700804	4.136048	1.296524

50	6	0	-2.543802	3.261181	1.863439
51	1	0	-2.340102	3.804360	2.797543
52	1	0	-3.066019	3.948928	1.184067
53	1	0	-3.231328	2.439128	2.094135

Table S9. Excitation energies and oscillator strengths calculated for **2'**.

Excited State 1: 2.012-A 1.0901 eV 1137.34 nm f=0.0412 <S**2>=0.762

124B ->125B 0.98494

Excited State 2: 2.014-A 1.0920 eV 1135.44 nm f=0.0000 <S**2>=0.764

116B ->125B -0.27982

123B ->125B 0.95099

Excited State 3: 2.014-A 1.4216 eV 872.17 nm f=0.0026 <S**2>=0.764

106B ->125B -0.17953

115B ->125B -0.14311

119B ->125B -0.14966

122B ->125B 0.95136

Excited State 4: 2.016-A 1.5197 eV 815.85 nm f=0.0004 <S**2>=0.766

117B ->125B -0.28839

119B ->125B 0.93398

122B ->125B 0.14766

Excited State 5: 2.014-A 1.7681 eV 701.21 nm f=0.0035 <S**2>=0.764

106B ->125B -0.12989

108B ->125B -0.21992

121B ->125B 0.95954

Excited State 6: 2.014-A 1.7853 eV 694.48 nm f=0.0001 <S**2>=0.764

103B ->125B -0.13558

110B ->125B -0.12442

120B ->125B 0.96831

Excited State 7: 2.018-A 2.0145 eV 615.45 nm f=0.0000 <S**2>=0.768

107B ->125B -0.11607

116B ->125B 0.31707

118B ->125B 0.91674

Excited State 8: 2.017-A 2.0629 eV 601.01 nm f=0.0000 <S**2>=0.767

107B ->125B -0.17133

114B ->125B -0.38394

116B ->125B 0.82481

118B ->125B -0.28052

123B ->125B 0.23153

Excited State 9: 2.009-A 2.1445 eV 578.16 nm f=0.1373 <S**2>=0.759

117B ->125B 0.92381

119B ->125B 0.28993

Excited State 10: 2.019-A 2.1931 eV 565.35 nm f=0.0021 <S**2>=0.770

106B ->125B -0.10521

115B ->125B 0.97445

122B ->125B 0.12177

Excited State 11: 2.021-A 2.2968 eV 539.81 nm f=0.0006 <S**2>=0.771

113B ->125B -0.41552
114B ->125B 0.81505
116B ->125B 0.25767
118B ->125B -0.18268
123B ->125B 0.12055

Excited State 12: 2.023-A 2.3075 eV 537.30 nm f=0.0024 <S**2>=0.773

101B ->125B 0.14150
103B ->125B 0.16943
113B ->125B 0.86179
114B ->125B 0.39427
116B ->125B 0.13180

Excited State 13: 2.022-A 2.3845 eV 519.95 nm f=0.0022 <S**2>=0.772

108B ->125B 0.20952
112B ->125B 0.96306

Excited State 14: 2.022-A 2.5655 eV 483.27 nm f=0.0004 <S**2>=0.772

110B ->125B -0.50719
111B ->125B 0.84862

Excited State 15: 2.021-A 2.6971 eV 459.70 nm f=0.0000 <S**2>=0.771

103B ->125B -0.22846
110B ->125B 0.81149
111B ->125B 0.49847
120B ->125B 0.11851

Excited State 16: 2.024-A 2.7419 eV 452.18 nm f=0.0011 <S**2>=0.774

108B ->125B -0.15892

109B ->125B 0.96425

Excited State 17: 2.027-A 2.7674 eV 448.02 nm f=0.0002 <S**2>=0.778

108B ->125B 0.91836

109B ->125B 0.17454

112B ->125B -0.20170

121B ->125B 0.22317

122B ->125B -0.11180

Excited State 18: 2.026-A 2.8010 eV 442.65 nm f=0.0000 <S**2>=0.776

105B ->125B 0.65387

107B ->125B 0.72969

116B ->125B 0.10957

Excited State 19: 2.028-A 2.9282 eV 423.41 nm f=0.0000 <S**2>=0.778

105B ->125B 0.73661

107B ->125B -0.62098

116B ->125B -0.17680

123B ->125B -0.11599

Excited State 20: 2.026-A 2.9584 eV 419.09 nm f=0.0004 <S**2>=0.776

104B ->125B 0.97627

106B ->125B 0.15190

Excited State 21: 2.023-A 3.0904 eV 401.20 nm f=0.0009 <S**2>=0.773

102B ->125B -0.16140

104B ->125B -0.14710

106B ->125B 0.93325

121B ->125B 0.12978

122B ->125B	0.19626
Excited State 22: 2.027-A	3.1250 eV 396.74 nm f=0.0044 <S**2>=0.777
102B ->125B	0.96600
106B ->125B	0.15586
Excited State 23: 2.865-A	3.1862 eV 389.13 nm f=0.0000 <S**2>=1.802
124B ->126B	0.96849
124B ->130B	-0.17849
Excited State 24: 2.032-A	3.2040 eV 386.96 nm f=0.0002 <S**2>=0.783
125A ->126A	0.97670
125A ->130A	0.12024
Excited State 25: 2.025-A	3.2162 eV 385.50 nm f=0.0026 <S**2>=0.775
101B ->125B	-0.16399
103B ->125B	0.92412
110B ->125B	0.19048
113B ->125B	-0.14148
120B ->125B	0.19548

Table S10. Excitation energies and oscillator strengths calculated for **1'**.

Excited State 1: Singlet-A	0.8195 eV 1512.85 nm f=0.0000 <S**2>=0.000
124 ->125	0.69812
Excited State 2: Singlet-A	0.9557 eV 1297.26 nm f=0.0002 <S**2>=0.000
120 ->125	-0.12684

122 ->125 0.34619

123 ->125 0.59919

Excited State 3: Singlet-A 1.1420 eV 1085.69 nm f=0.0089 <S**2>=0.000

120 ->125 0.21827

122 ->125 0.59859

123 ->125 -0.30230

Excited State 4: Singlet-A 1.1876 eV 1044.00 nm f=0.0005 <S**2>=0.000

121 ->125 0.70440

Excited State 5: Singlet-A 1.6223 eV 764.26 nm f=0.0038 <S**2>=0.000

118 ->125 -0.32957

119 ->125 0.62069

Excited State 6: Singlet-A 2.0442 eV 606.51 nm f=0.0000 <S**2>=0.000

113 ->125 0.10210

116 ->125 -0.48352

117 ->125 0.48766

124 ->125 0.10386

Excited State 7: Singlet-A 2.1103 eV 587.53 nm f=0.1047 <S**2>=0.000

115 ->125 -0.14336

120 ->125 0.64006

122 ->125 -0.12524

123 ->125 0.21890

120 <-125 -0.11134

Excited State 8: Singlet-A 2.4436 eV 507.39 nm f=0.0163 <S**2>=0.000

115 ->125 0.68200

120 ->125 0.12697

Excited State 9: Singlet-A 2.5187 eV 492.26 nm f=0.0000 <S**2>=0.000

113 ->125 0.66734

116 ->125 0.19973

Excited State 10: Singlet-A 2.5267 eV 490.71 nm f=0.0111 <S**2>=0.000

100 ->125 -0.13704

104 ->125 -0.12763

114 ->125 0.66842

Excited State 11: Singlet-A 2.6557 eV 466.86 nm f=0.3389 <S**2>=0.000

112 ->125 -0.10268

118 ->125 0.60542

119 ->125 0.31790

Excited State 12: Singlet-A 2.6650 eV 465.23 nm f=0.0000 <S**2>=0.000

108 ->125 -0.14988

113 ->125 -0.18960

116 ->125 0.43924

117 ->125 0.47689

Excited State 13: Singlet-A 2.8013 eV 442.60 nm f=0.0123 <S**2>=0.000

107 ->125 0.18044

110 ->125 0.66256

120 ->125 0.10742

Excited State 14: Singlet-A 2.8478 eV 435.36 nm f=0.0010 <S**2>=0.000

109 ->125 0.43980

111 ->125 0.54322

Excited State 15: Singlet-A 2.9437 eV 421.19 nm f=0.0006 <S**2>=0.000

101 ->125 -0.12153

104 ->125 -0.20509

109 ->125 0.50894

111 ->125 -0.42265

Excited State 16: Singlet-A 2.9488 eV 420.45 nm f=0.0018 <S**2>=0.000

112 ->125 0.68901

Excited State 17: Singlet-A 2.9848 eV 415.39 nm f=0.0034 <S**2>=0.000

107 ->125 0.66881

110 ->125 -0.19805

Excited State 18: Singlet-A 3.1279 eV 396.38 nm f=0.0000 <S**2>=0.000

103 ->125 0.14705

108 ->125 0.66723

116 ->125 0.11342

Excited State 19: Singlet-A 3.2227 eV 384.72 nm f=0.0006 <S**2>=0.000

105 ->125 0.56403

106 ->125 -0.41055

Excited State 20: Singlet-A 3.2489 eV 381.62 nm f=0.0001 <S**2>=0.000

105 ->125 0.40875

106 ->125 0.56155

Excited State 21: Singlet-A 3.3478 eV 370.35 nm f=0.0000 <S**2>=0.000

103 ->125 0.68142

108 ->125 -0.12975

Excited State 22: Singlet-A 3.3857 eV 366.19 nm f=0.0043 <S**2>=0.000

101 ->125 -0.20671

104 ->125 0.64012

109 ->125 0.13061

Excited State 23: Singlet-A 3.5036 eV 353.88 nm f=0.0152 <S**2>=0.000

102 ->125 0.68398

Excited State 24: Singlet-A 4.0030 eV 309.73 nm f=0.0000 <S**2>=0.000

120 ->126 0.12598

122 ->126 -0.18612

123 ->126 0.66239

Excited State 25: Singlet-A 4.0195 eV 308.46 nm f=0.0032 <S**2>=0.000

124 ->126 0.69794

Excited State 26: Singlet-A 4.0779 eV 304.04 nm f=0.0000 <S**2>=0.000

122 ->126 0.66474

123 ->126 0.18888

Excited State 27: Singlet-A 4.2220 eV 293.66 nm f=0.0769 <S**2>=0.000

121 ->126 0.69025

Excited State 28: Singlet-A 4.2988 eV 288.42 nm f=0.0372 <S**2>=0.000

98 ->125 0.10538

100 ->125 0.26640
101 ->125 0.56354
104 ->125 0.12178
109 ->125 0.14037
114 ->125 0.16931

Excited State 29: Singlet-A 4.4764 eV 276.97 nm f=0.0000 <S**2>=0.000

120 ->126 -0.29542
123 ->127 0.60347

Excited State 30: Singlet-A 4.4959 eV 275.77 nm f=0.0206 <S**2>=0.000

123 ->129 0.10267
124 ->127 0.68345

Excited State 31: Singlet-A 4.5198 eV 274.31 nm f=0.0094 <S**2>=0.000

89 ->125 0.25955
92 ->125 0.15191
94 ->125 0.11845
95 ->125 0.39205
99 ->125 0.46736

Excited State 32: Singlet-A 4.5363 eV 273.32 nm f=0.0000 <S**2>=0.000

96 ->125 -0.15886
97 ->125 0.25528
120 ->126 0.53293
122 ->127 -0.10522
123 ->127 0.25643

Excited State 33: Singlet-A 4.5538 eV 272.26 nm f=0.0000 <S**2>=0.000

120 ->126	0.10775
121 ->128	0.10769
122 ->127	0.66340
122 ->133	0.11466

Excited State 34: Singlet-A 4.6004 eV 269.51 nm f=0.0000 <S**2>=0.000

87 ->125	0.12315
90 ->125	0.26954
96 ->125	-0.27646
97 ->125	0.43600
120 ->126	-0.28827
123 ->127	-0.13393

Excited State 35: Singlet-A 4.6488 eV 266.70 nm f=0.0072 <S**2>=0.000

99 ->125	-0.11687
121 ->127	0.64920
121 ->133	0.10600
122 ->128	0.17017

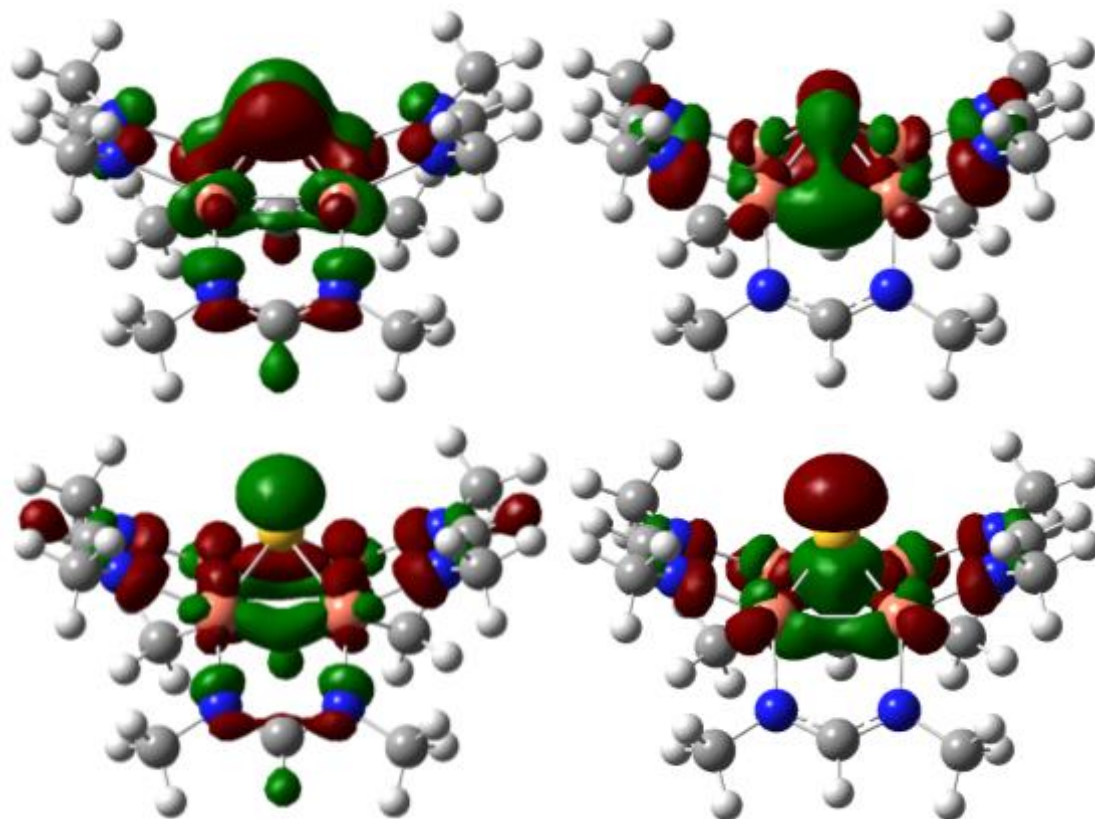


Figure S28. Frontier S(p) donor MOs for singlet 1': MOs 116-119 (i.e. HOMO-6 through HOMO-9; isovalue = 0.04).

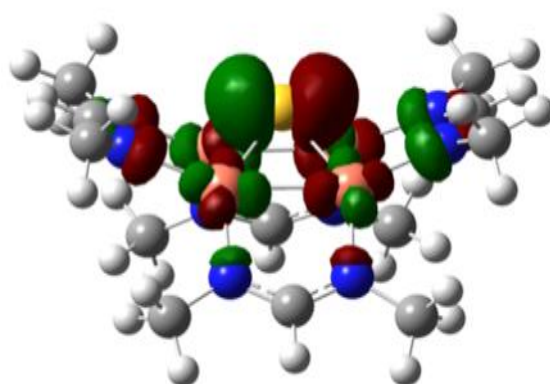


Figure S29. LUMO for singlet 1' (MO 125, isovalue = 0.04).

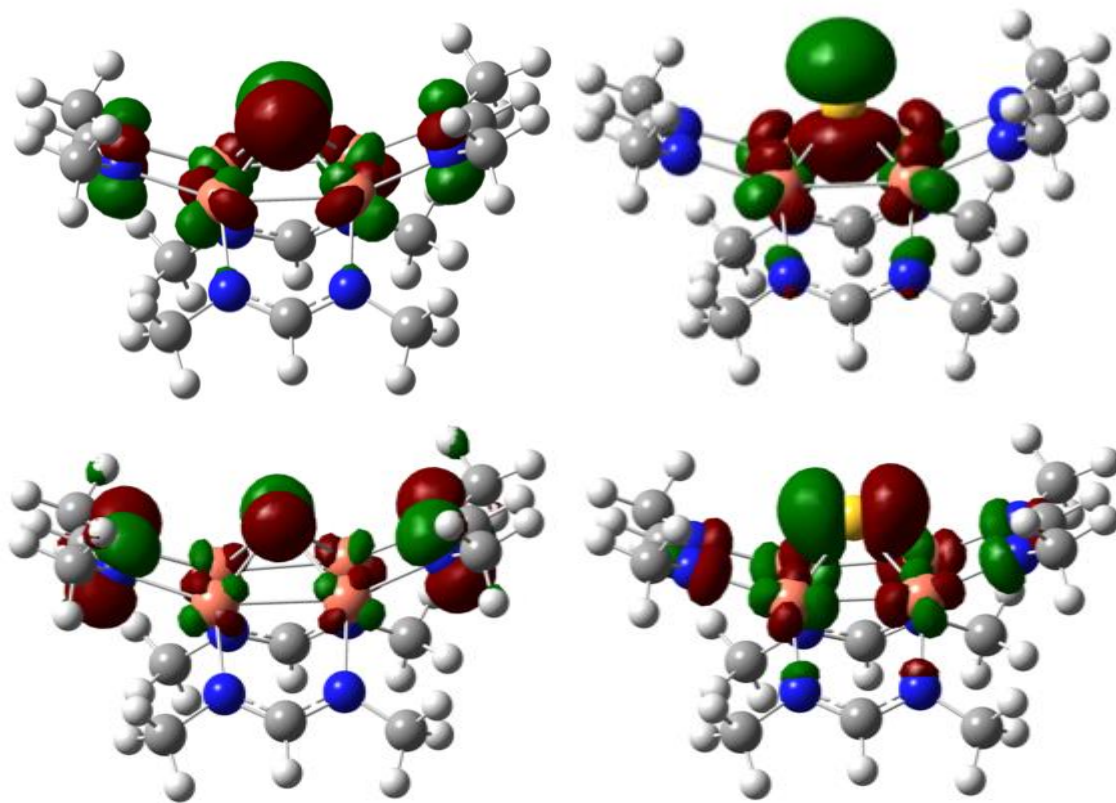


Figure S30. Filled S(p) α -MOs for singlet **1'**: MOs 118 α , 120 α , 124 α , 125 α (isovalue = 0.04).

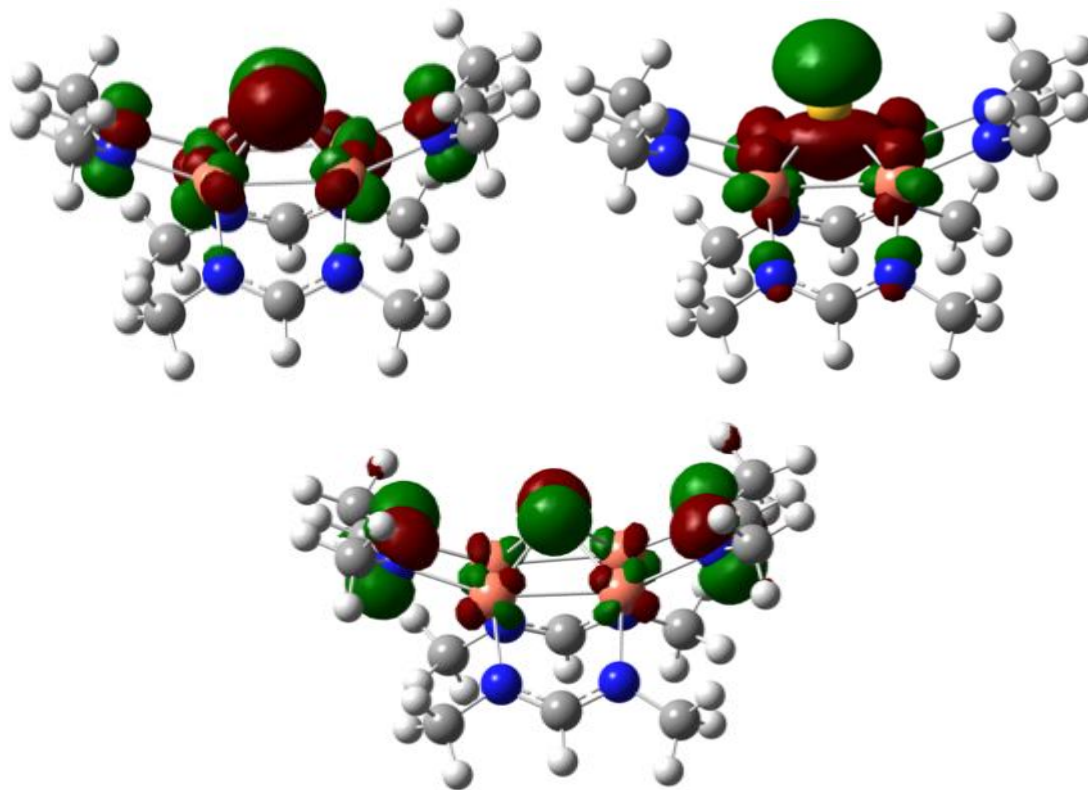


Figure S31. Filled S(p) β -MOs for singlet **1'**: MOs 116 β , 119 β , 123 β (isovalue = 0.04).

References Cited:

- ¹ Stoll, S.; Schweiger, A. J.; *J. Magn. Reson.* **2006**, *78*, 42.
- ² Sheldrick, G. M. *Acta Cryst.* **2008**, *A64*, 112–122
- ³ Dolomanov, O. V.; Bourhis, L. J.; Gildea, R. J.; Howard, J. A. K.; Puschmann, H. *J. Appl. Cryst.* **2009**, *42*, 339–341
- ⁴ Johnson, B. J.; Antholine, W. E.; Lindeman, S. V.; Mankad, N.P. *Chem. Commun.* **2015**, *51*, 11860.
- ⁵ Karunananda, M. K.; Vazquez, F. X.; Alp, E. E.; Bi, W.; Chattopadhyay, S.; Shibata, T.; Mankad, N. P. *Dalton Trans.* **2014**, *43*, 13361.
- ⁶ Frisch, M. J.; Trucks, G. W.; Schlegel, H. B.; Scuseria, G. E.; Robb, M. A.; Cheeseman, J. R.; Scalmani, G.; Barone, V.; Mennucci, B.; Petersson, G. A.; Nakatsuji, H.; Caricato, M.; Li, X.; Hratchian, H. P.; Izmaylov, A. F.; Bloino, J.; Zheng, G.; Sonnenberg, J. L.; Hada, M.; Ehara, M.; Toyota, K.; Fukuda, R.; Hasegawa, J.; Ishida, M.; Nakajima, T.; Honda, Y.; Kitao, O.; Nakai, H.; Vreven, T.; Montgomery, J. A., Jr.; Peralta, J. E.; Ogliaro, F.; Bearpark, M.; Heyd, J. J.; Brothers, E.; Kudin, K. N.; Staroverov, V. N.; Keith, T.; Kobayashi, R.; Normand, J.; Raghavachari, K.; Rendell, A.; Burant, J. C.; Iyengar, S. S.; Tomasi, J.; Cossi, M.; Rega, N.; Millam, J. M.; Klene, M.; Knox, J. E.; Cross, J. B.; Bakken, V.; Adamo, C.;

-
- Jaramillo, J.; Gomperts, R.; Stratmann, R. E.; Yazyev, O.; Austin, A. J.; Cammi, R.; Pomelli, C.; Ochterski, J. W.; Martin, R. L.; Morokuma, K.; Zakrzewski, V. G.; Voth, G. A.; Salvador, P.; Dannenberg, J. J.; Dapprich, S.; Daniels, A. D.; Farkas, O.; Foresman, J. B.; Ortiz, J. V.; Cioslowski, J.; Fox, D. J. *Gaussian 09, Revision B.01*; Gaussian, Inc., Wallingford, CT, 2010.
- ⁷ (a) Becke, A. D. *J. Chem. Phys.* **1993**, *98*, 5648-5652. (b) Lee, C.; Yang, W.; Parr, R. G. *Phys. Rev. B* **1988**, *37*, 785-789. (c) Vosko, S. H.; Wilk, L.; Nusair, M. *Can. J. Phys.* **1980**, *58*, 1200-1211. (d) Stephens, P. J.; Devlin, F. J.; Chabalowski, C. F.; Frisch, M. J. *J. Phys. Chem.* **1994**, *98*, 11623-11627.
- ⁸ (a) Hay, P. J.; Wadt, W. R. *J. Chem. Phys.* **1985**, *82*, 299. (b) Roy, L. E.; Hay, P. J.; Martin, R. L. *J. Chem. Theory Comput.* **2008**, *4*, 1029. (c) Ehlers, A. W.; Bohme, M.; Dapprich, S.; Gobbi, A.; Hollwarth, A.; Jonas, V.; Kohler, K. F.; Stegmann, R.; Veldkamp, A.; Frenking, G. *Chem. Phys. Lett.* **1993**, *208*, 111.
- ⁹ (a) Hay, P. J.; Wadt, W. R. *J. Chem. Phys.* **1985**, *82*, 270. (b) Hay, P. J.; Wadt, W. R. *J. Chem. Phys.* **1985**, *82*, 284. (c) Hay, P. J.; Wadt, W. R. *J. Chem. Phys.* **1985**, *82*, 299.
- ¹⁰ Tomasi, J.; Mennucci, B.; Cammi, R. *Chem. Rev.* **2005**, *105*, 2999-3093.
- ¹¹ Martin, R. L. *J. Chem. Phys.* **2003**, *118*, 4775.
- ¹² Dennington, R.; Keith, T.; Millam, J. *GaussView, Version 4.1*; Semichem Inc., Shawnee Mission, KS, 2009.